CFD Icing Simulations on Rotors for eVTOL Unmanned Aircraft

Master's thesis

by

Henidya Putri Heramarwan

Institut für Aerodynamik und Gasdynamik

Universität Stuttgart

&

Department of Engineering Cybernetics

Norwegian University of Science and Technology

Trondheim, in March 2023

Masterarbeit
für Frau Henidya Heramarwan
(durchgeführt an der NTNU, Norwegen)

CFD icing simulations on rotors for eVTOL unmanned aircraft

A key limitation to the operational envelope of unmanned aerial vehicles (UAVs) today is the risk of atmospheric in-flight icing. In contrast to icing in manned aviation, UAV icing is not well established and is an emerging research topic. The Norwegian University of Science and Technology (NTNU) is offering a master thesis on the topic of icing on rotors of electric vertical take-off and landing (eVTOL) unmanned aircraft.

The main objective of this project is to run icing computational fluid dynamics (CFD) simulations on lift rotors. Simulations are to be conducted with ANSYS FENSAP-ICE. Mesh generation will be conducted in Pointwise based on an existing geometry. The simulations will compute ice accretion on rotor blades and analyze the effect on lift and thrust. Furthermore, the simulations will estimate the required anti-icing heat fluxes to protect the blades against icing. The outcome of this thesis will be used to assess the sensitivity of the eVTOL unmanned aircraft to icing in comparison to conventional fixed-wing UAVs.

The thesis is to be conducted in English at the NTNU UAV Icing Lab in Trondheim.

Tasks:

- Literature study on aircraft icing, UAV icing, and rotor icing.
- 3D mesh generation in Pointwise based on an existing CAD model and mesh convergence study.
- CFD simulations of ice accretion on an eVTOL rotor with ANSYS FENSAP-ICE in 3D.
- Comparison of numerical ice shape results to experimental results for validation.
- Simulation of different types of icing conditions (rime, glaze, mixed).
- Assess the effect of ice accretion on the rotor performance.
- Estimate anti-icing loads on the rotor.
- Critical discussion of results.

Die Arbeit wird an der NTNU in Trondheim (Norwegen) durchgeführt.

Betreuer seitens NTNU:	Dr. Richard Hann
Betreuer seitens des IAGs:	Dr.-Ing. Thorsten Lutz, MSc. Mário Firnhaber-Beckers
Ausgabetermin:	8.8.2022
Spätester Abgabetermin:	7.2.2023

Dr.-Ing. Thorsten Lutz

Erklärung

Hiermit versichere ich, dass ich diese Masterarbeit selbstständig mit Unterstützung des Betreuers / der Betreuer angefertigt und keine anderen als die angegebenen Quellen und Hildsmittel verwendet habe.
Die Arbeit oder wesentliche Bestandteile davon sind weder an dieser noch an einer anderen Bildungseinrichtung bereits zur Erlangung eines Abschlusses eingereicht worden.
Ich erkläre weiterhin, bei der Erstellung der Arbeit die einschlägigen Bestimmungen zum Urheberschutz fremder Beiträge entsprechend den Regeln guter wissenschaftlicher Praxis eingehalten zu haben. Soweit meine Arbeit fremde Beiträge (z.B. Bilder, Zeichnungen, Textpassagen etc.) enthält, habe ich diese Betiräge als solche gekennzeichnet (Zitat, Quellenangabe) und eventuell erforderlich gewordene Zustimmungen der Urheber zur Nutzung dieser Beiträge in meiner Arbeit eingeholt. Mir ist bekannt, dass ich im Falle einer schuldhaften Verletzung dieser Pflichten die daraus entstehenden Konsequenzen zu tragen habe.

....
Ort, Datum, Unterschrift

Statement of Orginality

This thesis has been performed independently with support of my supervisor/s. It contains no material that has been accepted for the award of a degree at this or any other university. To the best of my knowledge and belief, this thesis contains no material previously published or written by another person except where due reference is made in the text.
I further declare that I have performed this thesis according to the existing copyright policy and the rules of good scientific practice. In case this works contains contributions of someone else (e.g. pictures, drawings, text passages etc.), I have clearly identified the source of these contributions, and, if necessary, have obtained approval from the originator for making use of them in this thesis. I am aware that I have to bear the consequences in case I have contravened these duties.

....
Place, Date, Sign

Acknowledgements

The numerical simulations were performed on resources provided by the National Infrastructure for High Performance Computing and Data Storage in Norway (UNINETT Sigma2) on the Fram supercomputer, under project code NN9613K Notur/NorStore. I would also like to thank ERASMUS+ for the financial aid awarded during my stay abroad.

This thesis would not have been finished without the support and guidance of my supervisors: Dr. Richard Hann, Dr. Thorsten Lutz, Nicolas Müller, and Mário Firnhaber-Beckers. It has been an eventful past couple of months, filled with many learning opportunities and perspective changes and I want to thank Richard especially for giving me this opportunity. My special thanks go to Nico for showing me the nooks and crannies of FENSAP-ICE and Pointwise. I appreciate your input and everything you have taught me over the past months.

I want to thank my family for their endless support. To my friends, be it in Germany or Indonesia, thank you for being there for me even when it's only through social media. And to my Erasmus friends and office mates in Trondheim, thank you for making my exchange semester even more memorable.

Last but far from least, I would like to express my heartfelt gratitude to Falk Beisecker, to whom this thesis is dedicated. Words cannot describe how much I cherish having you in my life. Thank you for believing in me, especially in times when even I don't believe in myself.

Contents

Nomenclature

Latin

a	[m/s]	Speed of sound
A	[m^2]	Area
$c_{d\_droplet}$	[-]	Droplet drag coefficient
CFL	[-]	Courant-Friedrichs-Lewy number
F	[-]	Flux vector
Fr	[-]	Froude number
F_s	[-]	Safety factor
GCI	[-]	Grid convergence index
h_f	[mm]	Water film thickness
K	[-]	Droplet inertia
LWC	[g/m^3]	Liquid water content
Ma	[-]	Mach number
MVD	[μm]	Median volume diameter
p	[-]	Order of grid convergence
Q	[-]	Conservation equation on element
Q	[-]	Vector of conserved variable
r	[-]	Refinement ratio
R	[J/K mol]	Universal gas constant
Re	[-]	Reynolds number
Re_d	[-]	Droplet Reynolds number
R_i	[-]	Residual of an element vertex
T	[°C]	Temperature
$\tilde{u}_i$	[m/s]	Mean velocity
u_a	[m/s]	Air velocity
u_d	[m/s]	Droplet velocity
u_i	[m/s]	Velocity vector
u_i''	[m/s]	Fluctuating velocity components
V	[m^3]	Capacity of control volume element
V^e	[m^3]	Element volume
v_1	[m/s]	Induced velocity
W	[-]	Weight factor
x, y, z	[m]	Cartesian coordinates
y+	[-]	Dimensionless wall distance

Greek

α	[-]	Water volume fraction
κ	[-]	Adiabatic index
μ_t	[m^2/s]	Eddy viscosity
μ_w	[kg/ms]	Dynamic viscosity
ρ	[kg/m^3]	Density
ρ_w	[kg/m^3]	Water density
τ_{wall}	[Pa]	Shear stress from the air

Abbreviation

AAM	Advanced air mobility
AERTS	Adverse environment rotor test stand
CAD	Computer-aided design
eVTOL	Electric vertical take-off and landing
FAA	Federal aviation administration
FE	Fully evaporative
IPS	Ice protection system
IWT	Icing wind tunnel
RPM	Rotations per minute
RW	Running wet
UAM	Urban air mobility
UAV	Unmanned aerial vehicle
VTOL	Vertical take-off and landing
VTT	Technical research center of Finland

List of Figures

List of Tables

Abstract

Urban air mobility (UAM) is a growing industry with great prospects. This new aviation ecosystem utilizes electric take-off and landing (eVTOL) technologies to operate in areas with limited space. Cargo delivery would use UAVs with VTOL capabilities, while passenger transport is done using new eVTOL aircraft configurations designed especially for UAM purposes. The industry envisions a fully autonomous operation in the long term. This promising growth is not unchallenged. Atmospheric icing poses a key limitation to a UAM aircraft's operational envelope, safety, reliability, and availability. In-flight icing occurs when supercooled water droplets in the air hit an aircraft during flight and freeze onto the aerial vehicle. Ice formation changes the airflow behavior surrounding the geometry and it can happen anywhere around the globe regardless of the time of year. It is a well-known phenomenon in larger manned aviation, but still an emerging field for smaller and newer aircraft configurations. There have been increasing studies done to investigate the effects of icing on UAV wings and propellers. However, there is not much done on UAV rotors and even less on mid- to large-sized rotors suitable for UAM passenger aircraft. This thesis aims to contribute to closing this gap of knowledge.

Two rotor geometries were chosen for this study. A small 15-inch rotor was selected to illustrate a multirotor UAV drone, while a large 80-inch rotor was chosen to represent a UAM passenger aircraft. Three types of icing simulations were conducted: ice accretion, performance degradation, and anti-icing loads simulation, and all were performed using FENSAP-ICE from ANSYS. The ice accretion model was validated using experimental data from a scaled helicopter rotor. The ice accretion simulations of the 15-inch rotor sections at -5 °C show a large, rather streamlined ice shape instead of the expected glaze ice characteristics. This contradicts previous work on a UAV propeller, which shows distinct horn ice formation for this icing condition. At -15 °C the numerical ice accretion presents the typical rime ice shape. The results are generally similar to the ice shapes obtained from an experimental campaign in an icing wind tunnel. This would imply, that the rotational axis of the rotor with regard to the flow influences the ice accretion process. The results of the 80-inch rotor simulation present more varied ice shapes, which could indicate higher sensitivity towards the icing condition. Ice horns formed at temperatures close to freezing and the flow separation aft of the ice led to significant aerodynamic penalties. The 3D ice accretion simulation of the 80-inch rotor shows discrepancies with the 2D results as it does not predict ice accretion at the outer region of the blades at -15 °C. This could be due to the higher stagnation temperature, increased friction, and three-dimensional crossflows preventing ice accumulation. This behavior has been observed on larger manned aircraft. This could suggest that a UAM rotor with an 80-inch diameter tends to behave less like a UAV and more like a larger manned aircraft. The performance degradation simulations show that ice accretion causes significant aerodynamic

penalties, especially in cases where horn ice accretion forms. Determining the parameters influencing horn ice accretion would be essential to further study the extent of performance deterioration due to icing. Finally, the anti-icing loads required to thermally mitigate ice accretion were calculated. Both rotors require high power consumption for a fully evaporative IPS design. Several strategies could be looked into as an effort to lower the power requirements of the IPS.

Kurzfassung

Die urbane Luftmobilität (UAM) ist ein wachsender Industriesektor mit großen Zukunftsaussichten. Dieses neue Luftfahrt-Ökosystem setzt elektrische Start- und Lande-Technologien (eVTOL) ein, um in Regionen mit begrenztem Platz zu fliegen. Für die Güterbeförderung werden UAVs mit VTOL-Fähigkeiten eingesetzt, während für die Personenbeförderung neue eVTOL-Flugzeugkonfigurationen verwendet werden, die speziell für den UAM-Bereich entwickelt wurden. Langfristig stellt sich die Branche einen völlig autonomen Betrieb vor. Dieses aussichtsreiche Wachstum ist nicht ohne Herausforderungen. Die atmosphärische Vereisung stellt eine wesentliche Einschränkung für den Einsatzbereich, die Sicherheit, die Zuverlässigkeit und die Verfügbarkeit eines UAM-Flugzeugs dar. Vereisung während des Fluges tritt auf, wenn unterkühlte Wassertröpfchen in der Atmosphäre auf ein Flugzeug im Flug treffen und auf dem Fahrzeug einfrieren. Die Eisbildung verändert das Strömungsverhalten und dies kann unabhängig von der Jahreszeit überall auf der Welt auftreten. Es ist ein bekanntes Phänomen in der bemannten Luftfahrt, aber bei kleineren und neueren Flugzeugkonfigurationen ist es ein neu entstehendes Feld. Es wurden zunehmend Studien durchgeführt, um die Auswirkungen der Vereisung auf UAV-Flügel und Propeller zu untersuchen. Es gibt jedoch nur wenige Studien über UAV-Rotoren und noch weniger über mittelgroße bis große Rotoren, die für UAM-Passagierflugzeuge geeignet sind. Ziel dieser Arbeit ist es, einen Teil dazu beizutragen, diese Wissenslücke zu schließen.

Für diese Studie wurden zwei unterschiedliche Rotorgrößen ausgewählt. Ein kleiner 15x5-Zoll-Rotor wurde verwendet, um eine Multirotor-Drohne darzustellen, während ein großer 80x28-Zoll-Rotor für ein UAM-Passagierflugzeug gewählt wurde. Es wurden drei Arten von Vereisungssimulationen durchgeführt: Eisbildung, Leistungsverlust und Simulation von Anti-Icing-Lasten. Alle wurden mit FENSAP-ICE von ANSYS durchgeführt. Das Eisbildung-Modell wurde anhand experimenteller Daten eines skalierten Hubschrauberrotors validiert. Die Simulationsergebnisse zur Eisbildung zeigen eine große, eher stromlinienförmige Eisform auf den Profilen des kleinen Rotors bei -5 °C, anstatt der erwarteten Glaze-Eis-Eigenschaften. Dies widerspricht früheren Studien an einem UAV-Propeller, die für diese Vereisungsbedingung eine ausgeprägte Horn-Eisform zeigen. Bei -15 °C zeigt die numerische Eisbildung die typische Rime-Eisform. Die Ergebnisse ähneln im Allgemeinen den Eisformen, die bei einer experimentellen Untersuchung in einem Vereisungswindkanal ermittelt wurden. Dies deutet darauf hin, dass die Rotationsachse des Rotors den Eisbildungsprozess beeinflusst. Die Ergebnisse der Simulation des 80-Zoll-Rotors zeigen vielfältigere Eisformen, was auf eine höhere Empfindlichkeit gegenüber Vereisungsbedingungen hinweisen könnte. Eishörner, die sich bei Temperaturen nahe dem Gefrierpunkt bilden, und die Strömungsablösung hinter dem Eis führen zu erheblichen aerodynamischen Verlusten. Die 3D-Eisbildungssimulation des 80-Zoll-Rotors zeigt Abweichungen von den 2D-Ergebnissen, da sie die Eisbildung im äußeren Bereich der

Rotorblätter bei -15 °C nicht vorhersagt. Dies könnte auf die höhere Staupunkttemperatur zurückgeführt werden, die eine Eisbildung verhindert. Dieses Verhalten wurde bereits bei größeren bemannten Flugzeugen beobachtet. Dies könnte darauf hindeuten, dass sich ein UAM-Rotor mit einem Durchmesser von 80 Zoll weniger wie eine Drohne und mehr wie ein größeres bemanntes Flugzeug verhält. Die Simulationen zur Verringerung der Leistung zeigen, dass die Eisbildung zu erheblichen aerodynamischen Nachteilen führt, insbesondere in Fällen, in denen sich ein Horn-Eisform bildet. Die Bestimmung der Parameter, die die Horn-Eisbildung beeinflussen, wäre für die weitere Untersuchung des Ausmaßes der Leistungsverschlechterung aufgrund von Vereisung von wesentlicher Bedeutung. Schließlich wurden die Anti-Icing-Lasten berechnet, die erforderlich sind, um die Eisbildung thermisch abzumildern. Beide Rotoren benötigen einen hohen Energieverbrauch für ein IPS-Design. Es könnten mehrere Strategien in Betracht genommen werden, um den Leistungsbedarf des IPS zu senken.

1 Introduction

In this chapter, an introduction to this thesis is given. First, the motivation of this work and the state of the art are presented. It is followed by an overview of the study objectives. Finally, the thesis outline is described in the last subsection.

1.1 Motivation and State of the Art

Flying is said to be one of humanity's oldest dreams. Aside from depictions of winged gods and flying mythological creatures [1], the earliest references of vertical flight trace back to 400 BC in China in the form of a bamboo toy rotor, in which the shaft is spun by hand and flies upon release [2]. The toy inspired early flying devices, such as Mikhail Lomonosov's spring-driven coaxial rotor in 1743, and George Cayley's two-propeller experiment in 1792 [3]. The earliest quadrocopter experiment was done by Louis and Jacques Breguet in 1907, in which the pilot was lifted 0.6 m above ground for one minute [4]. The technological development of vertical flying rotorcraft has not stopped since then. In 1946, the Bell 47 became the first single-rotor light helicopter to be certified for civilian use [5]. Owing to their agility and maneuverability, helicopters have become integrated into daily life by the end of the 20th century, its application ranging from aerial cranes to emergency services. Interest in personal air vehicles showed in 2009 as NASA released a video rendering of its electric vertical take-off and landing (eVTOL) conceptual design dubbed the Puffin [6]. Research studies were conducted on this new concept [7, 8] and followed by several efforts from the industry sector such as the Airbus Vahana or the Bell Nexus 6HX. The rapid development of eVTOL technology is made possible by major advances in electric propulsion technology and the demand for new transportation systems, for example, the advanced air mobility (AAM) concept.

NASA envisions the AAM concept as a new aviation ecosystem using innovative and sustainable aircraft designs, which serve communities and regions previously unreachable or underserved by currently available transportation modes [9, 10]. It is an umbrella term overarching several other concepts such as urban air mobility (UAM) for the transportation of goods and passengers within a metropolitan area, regional air mobility for inter-city connections, cargo delivery using unmanned aerial vehicles (UAVs), ground infrastructure such as vertiports and landing pads, etc [11]. Aside from major aircraft manufacturers, several startups have made impactful developments in UAM aircraft design as plenty of first manned and unmanned flights were conducted from 2011 until today [12]. The UAM industry is projected to thrive. In a market study commissioned by NASA, Booz Allen Hamilton [13] predicted a market value worth a hundred billion US dollars for an unconstrained long-term market. Another market study by Roland Berger forecasted the market to reach up to 160 000 commercial flights by 2050 [14]. However, this growth is not a given as the industry is still facing operational hurdles [15]. One of them being atmospheric in-flight icing.

In-flight icing is a phenomenon that happens when supercooled water droplets exist in the air and upon collision can cause ice formation on an aircraft. The ice accumulation can affect either the aircraft engine [16] or the airframe [17], thus changing the airflow around the aircraft. The ice accretion rate is determined by both the vehicle parameters, e.g. size and flight velocity, and the meteorological conditions [15]. The Federal Aviation Regulations published documentation [18] concerning the definition of icing conditions to aid in the development of ice mitigation systems and for aircraft certification purposes. Four types of ice morphology can be observed: roughness, horn ice, streamwise and spanwise-ridge ice [19], and each type has different levels of severity. Previous studies show that icing conditions can exist any time of the year and anywhere around the globe [20, 21]. Some regions, such as Norway [22], are more prone to icing conditions. This imposes a significant restriction on an aircraft's availability as current regulations forbid operations in known icing conditions.

The problem with icing affects all sizes and configurations of manned and unmanned aviation. In larger manned aviation, the first icing studies started back in the 1940s [23]. A notable amount of research on the consequences of icing on aircraft systems has been conducted over the years [23–25]. While icing in manned aviation is considered well-established, the topic of icing on unmanned and other newer configurations is an emerging topic that still lacks comprehensive understanding. The first publicly available study on UAV icing was done by the United States Naval Air Development Center in 1990 [26], followed by other reports on icing-related UAV accidents [27, 28]. The topic of UAV icing wasn't addressed earlier due to the nature of early UAV applications being almost exclusively for military operations in hot humid environments [15]. As UAV applications become more integrated into modern life, the need for a better understanding of UAV icing and a mitigation system also increased. Several differences exist between the icing behavior in manned aviation and smaller aviation vehicles. This is due to the size and flight velocity difference, which consequently influences the flow regime. Larger manned aircraft typically operate at higher Reynolds numbers (Re $= 10^7 - 10^9$), whereas UAVs and smaller aircraft are situated in lower Reynold numbers (Re $= 10^5 - 10^7$) [29]. This difference heavily influences the ice accretion process [30]. Furthermore, there are notable challenges in computational fluid dynamic (CFD) icing studies for aircraft in the lower Reynolds regime [31]. Another difference between icing in larger and smaller aircraft is the flight velocity. Larger aircraft typically cruise with higher velocities. This leads to greater aerodynamic heating caused by viscous friction, which is often enough to counteract ice build-up at temperatures close to the freezing point. The aerodynamic heating of aircraft with slower velocities is often so low that it is negligible [15]. Smaller and thinner airfoils have higher droplet collision efficiency compared to larger and thicker airfoils [32], which lead to more power requirements for operation [33] and faster ice accretion [34]. The airfoil of eVTOL rotor blades is usually smaller and thinner compared to manned aviation.

In the last ten years, there has been more research work done on UAV icing [35–37]. However, there is still a lack of studies on eVTOL drone and aircraft rotors specifically. Previous research has shown that rotating lifting surfaces, such as rotors and propellers, are more sensitive to icing compared to fixed-wing [15]. This is owed to the higher relative airspeed at the tips of the blade and the smaller chord length and leading-edge diameter [32]. Another study on UAV propellers show a significant thrust reduction and power increase after a 100-second exposure to moderate icing conditions [33]. Research on a UAV rotor blade exhibits similar performance degradation [34]. Furthermore, the effect of centrifugal forces can lead to ice shedding, which increases the rotor imbalances [38]. With the before-mentioned aspects in consideration, closing this gap of knowledge is seen as a necessity. At the time of writing, one of the few ice protection systems (IPS) for UAVs currently in development is UBIQ Aerospace's electro-thermal system D·ICE [39]. There is no known ice mitigation system available for UAM aircrafts. To increase the availability, reliability and safety of an eVTOL aircraft, the rotor icing challenges must be addressed. This thesis aims to deliver a first insight into the ice accretion on eVTOL rotors and the corresponding performance reduction, also to assess the required anti-icing loads necessary to mitigate the problem.

1.2 Study Objective

Utilizing air space with means of advanced air mobility is a feasible option to make future transportation of passengers and cargo time-efficient, economic, reliable, and fossil-fuel free. This new transportation system is made possible by advances in eVTOL technology. Taking into account how atmospheric in-flight icing reduces availability, limits safety, and restricts the operational envelope of an eVTOL aircraft, further research into eVTOL icing is considered a necessity. To begin, the key differences between icing in traditional large manned aircraft and newer, typically smaller configurations drones be established. Then, CFD ice accretion simulations are run to obtain the numerical ice shapes of the rotors. The level of performance degradation of the iced rotor will depend on the ice accretion, which influences the flow around the rotor. Finally, the heat flux required for an ice mitigation system is calculated.

To summarize, the objectives of this thesis are listed below:

- Literature study on in-flight icing and eVTOL aircraft
- CFD ice accretion simulations
- Assess the effect of ice accretion on the rotor performance

- First estimation of the anti-icing loads

1.3 Thesis Outline

Following this introductory chapter, a brief explanation of the atmospheric icing process and eVTOL aircraft are presented in Chapter 2. The chapter includes a section depicting the difference between icing in larger manned aviation and smaller, newer aircraft configurations. The research methodology of this thesis is presented and described in Chapter 3. This chapter covers the numerical simulation method utilized in this study aircraft by the studied geometries, grid setup as well as the icing and flow conditions. The results of the simulations are described in Chapter 4. First, the results of the validation and the parameters used in the study are presented. Then the numerical ice shapes are described, followed by the performance degradation results and the required anti-icing loads. Chapter 5 presents a critical discussion of the obtained results, and a conclusion is given in Chapter 6.

2 Background

This chapter serves as an introduction to atmospheric icing, eVTOL aircraft, and the impact of icing on aircraft. The chapter begins with a brief introduction to in-flight icing, which can happen anywhere around the globe at any time of the year. The second subsection offers an overview of eVTOL aircraft, from their size to application and configuration. Finally, the impact of icing in manned and unmanned aviation is described in the last subsection.

2.1 Atmospheric In-Flight Icing

Atmospheric icing describes a phenomenon that occurs when water droplets with a temperature below the freezing point, also known as supercooled droplets, exist in the atmosphere [40]. It is also referred to as in-flight icing when an aircraft flies through this condition and the water droplets collide with the aircraft and form ice on the surface upon impact. Depending on the impingement location, icing can affect either the airframe structure of the aircraft [17], the engines [16], or both. This thesis focuses on rotor icing only. The shape and size of the ice accretion depend on the vehicle parameters, such as the size of the airframe and airspeed velocity, and the meteorological parameters, for example, liquid water content (LWC) and droplet size [15]. Bernstein et. al. [20, 21] has found that this phenomenon is possible all around the globe regardless of the time of the year, thus making in-flight icing a threat to an aircraft's safety. Considering that current regulations forbid flights into known icing conditions [41], in-flight icing is also a restriction to an aircraft's availability.

The icing process is divided into two steps: the droplet impingement and the freezing process [42]. To determine the impingement, the droplet trajectory must first be calculated. Small droplets tend to follow the airflow direction. This is owed to the droplet trajectory physics, which is determined by the balance between the droplet inertia and the aerodynamic forces acting on the droplet. In smaller droplets, the trajectory is for the most part determined by the aerodynamic forces. Meanwhile, for larger droplets, the inertial forces are dominant and the trajectory is more straight-lined. Consequently, larger droplets are more likely to collide with the aircraft. However, the size and form of an airfoil influence the degree to which the aerodynamic force on the airfoil can deflect the droplets. Small and thin airfoils have less impact on the flow field and therefore generate weaker aerodynamic forces compared to larger and thicker airfoils. As a result, small airfoils have higher collision efficiency than large airfoils [32]. After impingement, there is a freezing process which is defined by the thermal

(a) (b) (c)

Figure 2.1: The difference between rime (a), glaze (b), and mixed (c) ice shape types, images by courtesy of Richard Hann [40].

conduction between the airfoil surface and the impinging water as well as the heat transfer to the air. Icing increases the surface roughness of an airfoil, which influences the convective heat transfer and eventually lowers the surface temperature further [42]. It is a vicious cycle as lower surface temperatures lead to more ice accretion.

It is also important to note that the water freezing duration plays a role in the final ice shape. Droplets that freeze immediately upon impact will have a different shape compared to droplets that do not. There are three commonly observed icing types: rime, glaze, and mixed ice, which are illustrated in Figure 2.1. Rime ice is characterized by its opaque white color which comes from trapped air between the frozen water droplets. Typically, rime ice has a streamlined shape and the separation bubble aft of the ice is small. Therefore, the aerodynamic penalties are less severe [19]. Rime ice occurs in low temperatures where the impinging droplets freeze immediately upon collision. When the droplets do not immediately freeze, a thin water film is formed on the airfoil surface. This water film would either gradually freeze, which is called glaze ice or run back in the chord direction. Glaze ice typically occurs at temperatures near the freezing point. Glaze ice leads to high aerodynamic penalties [19], as the ice shape evolves irregularly and can develop ice horns, which cause large flow separation regions. Glaze ice appears clear as it does not contain trapped air. A combination of the two ice types is called mixed ice. As the ice formation depends on several parameters that often fluctuate within a short period, the ice shapes obtained in real life often contain characteristics of both rime and glaze ice. Mixed ice shape forms in a variety of shapes and it often causes more severe aerodynamic performance degradations [43].

Various wind tunnel experiments, flight tests, and numerical simulations [44] have shown, that ice formation leads to performance penalties. The accreting ice changes the geometry of the airfoil, which then alters the flow behavior. Typical aerodynamic penalties of icing include a change in the pitch moment, a decrease in the lift, an increase in drag, and a negative change in the stall angle. A decrease in lift translates to a higher power and thrust necessary for the aircraft to maintain flight [45]. Icing also negatively impacts the aircraft's stability and control [24]. A study on the performance of UAV airfoils in various icing conditions concluded that in the worst case at an icing temperature of -2 °C and an MVD of 20 μm, the ice accretion reduced the lift by 35% while drag is increased up to 400% [35]. For further details, Lynch and Khodadoust [24] and Bragg et al. [19] have provided an extensive study on the effects of ice accretion on aircraft aerodynamics and the flow physics.

2.2 eVTOL Aricraft

The term vertical take-off and landing (VTOL) characterizes an aircraft that can take off and land vertically, thus eliminating the need for a runway, and having hover capabilities. Aircraft types under this category include helicopters, thrust vectored fixed-wing jets such as British Aerospace's Sea Harrier, tiltrotor aircraft like the Bell Boeing V-22 Osprey, to gyrodynes [46]. An eVTOL is a subset of the VTOL, which specifically characterizes aircraft with VTOL capabilities and utilizes a form of electric propulsion. The past few years have seen rapid development in eVTOL technology. This is made possible by the recent advances in technology, from fuel cells to electric controllers, coupled with growing interest in the AAM sector [14]. NASA describes AAM as an overarching term for the new aviation ecosystem, which utilizes UAVs and new UAM aircraft for cargo and passenger transport [9].

Electric VTOL aircraft come in various shapes, sizes, and configurations as their design are mostly dictated by their intended application. Most recent eVTOL designs utilize either batteries or hydrogen fuel cells as a source of power. Some studies suggest using both in a hybrid architecture to enhance the maximum range [47]. There are several configurations commonly used in eVTOL aircraft design: vectored thrust, lift and cruise, multirotor and electric rotorcraft [48]. Thrust vectoring describes an aircraft's ability to manipulate the direction of thrust produced by its propulsion system [49]. An eVTOL aircraft with vectored thrust uses all or some of its thrusters for both lift and cruise. This configuration includes a tilting mechanism to change the rotation axis of the thrusters from parallel to orthogonal to the flight direction or vice versa. A lift and cruise configuration implements two different power trains for lift and cruise independent of each other so that no vectoring mechanism is necessary [50]. Multirotors utilize their thrusters exclusively for lift. Vectored thrust and lift and cruise eVTOL aircraft are typically combined with a fixed wing for generating lift during cruise flights. Most multirotor designs are wingless. Bacchini and Cestino [51] found in their study, that the multirotor design is most efficient for hover while the vectored thrust is more suitable for cruising with higher range. The Vertical Flight Society [52] provides an extensive directory of eVTOL aircraft categorized by their configuration. Taking the numerous possible configurations, specifying what kind of eVTOL aircraft studied is a necessity.

In the scope of this thesis, the studied eVTOL rotors are distinguished by size. A small eVTOL would refer to drones with VTOL capabilities, for example, a multirotor UAV, with an operational altitude below 500 ft above ground level [53]. Meanwhile, a large eVTOL is assumed to be eVTOL aircraft intended mainly for passenger transport and additionally for cargo delivery. Real-life examples would be the Joby S4 [54], Archer Midnight [55] or VoloCity [56] from Volocopter. A UAM passenger aircraft is thought to cruise at a flight altitude ranging from 1500 ft to 4000 ft above ground level [57]. In the sense of an AAM ecosystem, a small eVTOL's main application would be cargo delivery while a large eVTOL focuses on passenger transport in the framework of UAM, but not exclusively. To date, most commercial UAVs operate within visual line of sight with rotary wings [15]. However, there has been increased interest in UAV applications beyond the visual line of sight and either fully autonomous or remotely piloted. At the time of writing, most UAM aircraft designs introduced to the public are configured with a pilot on board. However, the long-term goal of most UAM service providers is to implement autonomous UAM aircraft to push down operational costs [10].

2.3 Icing in Different Aircraft Configurations

In-flight icing imposes a risk to all aircraft regardless of size and how it is piloted [15]. While icing is considered a well-known phenomenon in larger manned aviation, icing in smaller and newer configurations is still an emerging field [40]. Due to the different technical characteristics, the icing behavior of UAVs, and potentially UAM aircraft as well, differentiate from larger manned aviation. To start, ice detection on UAVs and autonomous aircraft relies on sensors as there is no pilot on board. This creates a demand for a high-fidelity ice detection system and a robust ice mitigation system for application in autonomous aircraft [15]. Second, there is a difference in the Reynolds number regime. Owing to its smaller size and flight velocity, an eVTOL aircraft operates in a low Reynolds number regime where laminar flow is dominant. This changes the physical properties of the flow [30] compared to larger manned aviation and makes the aircraft more sensitive to ice surface roughness [19].

It is also important to mention that most commercial UAVs and eVTOL UAM aircraft concept designs rely on some form of rotating lifting surface for generating thrust. The airfoil of eVTOL rotor blades is typically smaller and thinner than the rotors in manned aviation. This leads to a higher impingement rate and increased sensibility to ice accretion [32], which translates to increased power consumption of the rotor [33] and rapid ice accretion [34]. Studies show that propeller icing is worst in rime ice cases, while glaze ice has more severe penalties for fixed wing [58]. Another study has shown that the lower the icing temperature is, the greater the performance degradation appears [45]. Furthermore, the centrifugal forces acting on the iced blade can lead to ice shedding once a critical ice mass on the blade of the rotor is reached.

In general, ice shedding impacts the outer side of the blade more due to increased centrifugal force effects [38]. Ice shedding occurrence depends on the type of ice and the surface area of the ice buildup [59]. For fixed-wing aircraft, the shedding time is influenced significantly by the angle of attack [60]. Experiments on an iced propeller have shown that the lower the icing temperature is, the later the ice shed [45]. Considering the above-mentioned points, one can suggest that studying icing behavior on newer aircraft configurations is a pressing issue.

3 Methods

In this chapter, the methods used in this thesis are described. The chapter begins with a description of the numerical method utilized for the ice accretion simulations. The chosen verification and validation data are presented in the second part. The geometries used in this study are described in the third part and followed by an explanation of the grid setup. The grid dependency study is explained in the fourth part. Finally, the atmospheric icing conditions and the flow conditions used to set up the simulation are presented in the last parts.

3.1 Numerical Simulation

Since first developed in the 1970s, numerical simulation methods have been utilized in aerodynamic research. It has become an integral part of the development process; including investigating icing on certain designs and designing the corresponding ice protection system [44]. This subsection concentrates on the computational fluid dynamics (CFD) tools used in this study, which are based on the solution of the Navier-Stokes equations. By utilizing mathematical models and numerical approaches, CFD simulations can predict flow behavior with high accuracy. However, this comes with a relatively higher cost factor as correct implementation requires time, skills, and often high computational power. It is also important to note that the reliability of CFD simulation results depends on the input data and therefore requires validation with real-life data. A common way of conducting a CFD simulation is by discretizing the continuous flow field into nodes in a mesh. The time is also discretized into time steps. The physical attributes of the flow, which are characterized by the Navier-Stokes equations, are calculated in these nodes while the values in between the nodes are interpolated [61]. To simulate the fluctuating component of a flow field, a turbulence model is applied. In icing studies, it is also necessary to solve the water droplet impingement to provide information regarding the behavior of water droplets within the flow. Finally, with the data achieved from the flow and droplet solver, the ice accretion and water runback can be calculated.

There are several tools available specifically designed for ice accretion simulations [62]. However, most of these icing simulation tools are historically developed for use in larger manned aviation. As UAVs and UAM aircraft are smaller in size and cruise at lower airspeeds, they operate on a lower Reynolds number regime. Therefore, the application for newer aerial vehicles is not always within the software's validated range. The icing simulation tools commonly used for investigating UAV icing cases are the LEWICE code [63] from NASA and FENSAP-ICE [64] developed by ANSYS Inc. The LEWICE code requires low computational power as the 2D code is based on the panel method. FENSAP-ICE is a Navier-Stokes solver and it is used as a 3D aid-to-certification simulation system [65]. Previous studies [66] comparing the two codes show that both tools are equally capable of simulating rime ice cases. However, for glaze and mixed ice cases, LEWICE tends to deliver simplified ice shape results. Considering that an assessment of performance degradation and anti-icing requirements depend strongly on the produced ice shape, achieving accurate ice morphologies is crucial.

The ice accretion simulations conducted in this thesis were done using ANSYS FENSAP-ICE [64] version 22.1 for the 2D simulations and version 22.2 for the 3D simulations. The software system consists of several modules which offer a comprehensive and robust methodology for aerodynamic and icing studies [64]. There are three modules utilized in an ice accretion simulation: FENSAP, DROP3D, and ICE3D. Each module calculates different steps of the icing process. To improve the simulation, it is possible to divide the icing time into smaller segments, for example, a total icing time of 300 seconds is conducted in 10 steps with 30 seconds each. This is called a multi-shot simulation. A new mesh is generated between each step to incorporate the accumulated ice. The airflow and droplet impingement is also recalculated using the new mesh, which then produces a new layer of ice accretion on top of the existing one. The steps are done iteratively for the complete simulation. The interaction between the modules and the remeshing step is illustrated in Figure 3.1. A more detailed description of the FENSAP-ICE modules is offered in the following subsections.

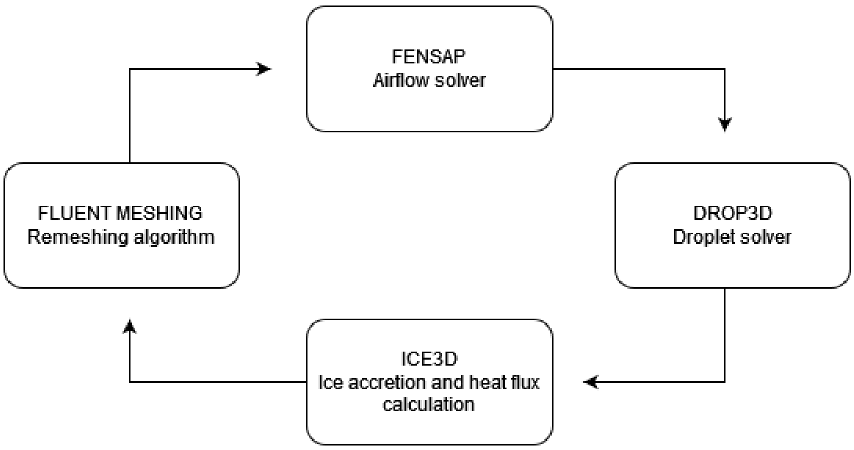

Figure 3.1: An illustration of the ice accretion simulation process in FENSAP-ICE based on [67] and including the remeshing step.

3.1.1 Navier-Stokes Equation and Flow Field Discretization

The airflow in this thesis is calculated using the Navier-Stokes equations, which describe numerous physics phenomena, especially of interest in scientific and engineering uses, from weather modeling, wind turbine load calculation to flow simulation. Unlike the Euler equations, which model only inviscid flow, the Navier-Stokes equations take viscosity into account thus describing the viscous flow [68]. The Navier-Stokes equations mathematically express the conservation of mass, the conservation of momentum of Newtonian fluids, and the conservation of energy as described in Equations 3.1, 3.2, and 3.3. The equations typically study three spatial dimensions and a time dimension. At present, the solution to the Navier-Stokes equations can only be approximated using numerical methods and a set of boundary conditions has to be implemented [68].

$$\frac{\partial \rho}{\partial t} + \frac{\partial (\rho u_i)}{\partial x_i} = 0 \tag{3.1}$$

$$\frac{\partial}{\partial t}(\rho u_i) + \frac{\partial}{\partial x_j}(\rho u_j U_j) = -\frac{\partial p}{\partial x_i} + \frac{\partial \tau_{ij}}{\partial x_j} \tag{3.2}$$

$$\frac{\partial}{\partial t}(\rho E) + \frac{\partial}{\partial x_j}(\rho u_j H) = \frac{\partial}{\partial x_j}(u_i \tau_{ij}) + \frac{\partial}{\partial x_j}\left(K \frac{\partial \tau}{\partial x_j}\right) \tag{3.3}$$

In CFD, the continuous flow field is discretized into a finite number of nodes forming a mesh. The physical properties of the flow are calculated only at the nodes and the results are interpolated for the remaining area [69]. As described by Munz and Westerman [70], there are several discretization methods typically used for calculating the Navier-Stokes equations. The works in this thesis use either the finite element method or the finite volume, which are commonly used in CFD solver algorithms. The finite element method uses the shape function as the weighting function, whereas the finite volume method is a specific case of the weighted residual method [71]. The finite element method, as described in the equation below,

$$R_i = \int\int\int W_i Q dV^e \tag{3.4}$$

has the advantage of being versatile for problems with complex geometry [72]. R_i in the equation describes the residual at an element vertex *i*, while *Q* depicts the conservation equation applied on an element basis. *W* and V^e express the weight factor and element volume, respectively. The finite element method solves partial differential equations by calculating the values of the conserved variables averaged across the volume [73]. The method is mathematically expressed as

$$\frac{\partial}{\partial t}\int\int\int Q dV + \int\int F dA = 0 \tag{3.5}$$

where *Q* defines the vector of the conserved variable, *F* being the flux vector, while *V* and *A* describe the capacity and surface area of the control volume element. In his book, Huebner et al. [74] stated that the finite element method requires higher computational power and longer calculation times compared to the finite volume method. Further details regarding the discretization methods can be found in the book by Munz and Westerman [70].

The airflow solution in this thesis is obtained by utilizing the FENSAP module from ANSYS. The FENSAP module is a state-of-the-art 3D finite element analysis package capable of solving various flow conditions such as compressible or incompressible, steady or unsteady, and viscous or inviscid in three-dimensional flow [75]. It can be used in a system, such as in FENSAP-ICE, or as a stand-alone module, for example, to calculate performance degradation. In this thesis, the airflow is set as steady state. The spatial discretization is done through a weak Galerkin finite element method [76]. Turbulence in the flow is modeled by applicating the Reynolds Averaged Navier-Stokes equations and a turbulence model, which will be further described in the next subsection. The flow field solution from FENSAP will be used to determine the droplet impingement in the DROP3D module, and the shear stress values are later taken to calculate the ice accretion in the ICE3D module of FENSAP-ICE.

3.1.2 Turbulence Modelling

Turbulence is often described as classical physics' most important unsolved problem [77]. Despite decades of research, at the time of writing, there is no detailed analytical theory available to predict the evolution of the turbulent flow. The Navier-Stokes equations can be solved as a whole, meaning that the entire spatial range and time scales of the turbulence must be calculated to capture all the dissipative scales [68]. This is called a direct numerical simulation. The method comes with very high computational costs, as it demands a very well-resolved mesh and an extremely fine time stepping. As an alternative to the direct numerical simulation, one can simplify the Navier-Stokes equations' solution variables by implementing the Reynolds Averaged Navier-Stokes (RANS) approach.

The RANS equations are time-averaged equations that divide the Navier-Stokes solution variables into the mean and fluctuating components. Several works of literature [78–80] recommend using the Favre decomposition for cases where the density is not constant. The velocity vector u_i can be described as

$$u_i = \tilde{u}_i + u_i'' \tag{3.6}$$

where $\tilde{u}_i$ stands for the mean velocity and u_i'' is the fluctuating velocity components. The average of the fluctuating component is equal to zero. By replacing the variables in the continuity and momentum equations with this expression, the averaged equations are achieved. This approach is called Favre-averaged. The Favre-averaged RANS equations in the Cartesian tensor form are expressed as

$$\frac{\partial \overline{\rho}}{\partial t} + \frac{\partial}{\partial x_i}(u_i) = 0 \tag{3.7}$$

$$\frac{\partial}{\partial t} + \frac{\partial}{\partial x_j}(\overline{\rho}\tilde{u}_i\tilde{u}_j) = \frac{\overline{p}}{\partial x_i} + \frac{\partial}{\partial x_j}\left[\mu\left(\frac{\partial \tilde{u}_i}{\partial x_j} + \frac{ial\tilde{u}_j}{\partial x_i}\right)\right] - \frac{\partial}{\partial x_j}\tilde{\tau}_{ij}^{RANS} \tag{3.8}$$

The left-hand side of Equation 3.8 describes the fluid momentum, while the right-hand side depicts the viscous stresses and the Favre-averaged Reynolds stress. The Reynolds stresses cannot be calculated directly and therefore require a model to close the equation. Joseph Boussinesq was the first to address this closure problem by presenting the concept of eddy viscosity. His hypothesis is applied to model the Reynolds stress term by implementing the eddy viscosity μ_t as a new parameter. The Boussinesq hypothesis is expressed as

$$-\tilde{\tau}_{ij}^{RANS} = \mu_t\left(\frac{\partial \tilde{u}_i}{\partial x_j} + \frac{\partial \tilde{u}_j}{\partial x_i}\right) - \frac{2}{3}\left(\overline{p}\tilde{k} + \mu_t\frac{\partial \tilde{u}_k}{\partial x_k}\right)\delta_{ij} \tag{3.9}$$

Turbulence models based on this hypothesis are therefore classified as large eddy viscosity models. Depending on how the eddy viscosity μ_t is determined, the models are further categorized as one- or two-equation models.

There are various turbulence models available for CFD simulations. NASA Langley Research Center [81] provides extensive documentation of turbulence models online. There are three turbulence models implemented in FENSAP-ICE: Spalart-Allmaras [82], low Reynolds $k - \omega$ [83] and Menter's $k - \omega$ SST model [84]. The simulations in this thesis are performed using the Spalart-Allmaras turbulence model, which is a one-equation model based on the transport of a modified eddy viscosity [65]. Ozcer et al. [85] prefer utilizing the Spalart-Allmaras turbulence model, especially for multishot simulations as the model performs well when calculating turbulence and heat transfer on iced surfaces. The simulations are configured as fully turbulent. This decision is made, as the increased surface roughness due to ice would cause the transition from laminar to turbulent boundary layer to happen at the leading edge [19].

3.1.3 Droplet Impingment

In-flight icing occurs when supercooled water droplets in the airflow collide with an aircraft and freezes upon impact. After solving the airflow, it is necessary to calculate the droplet trajectory before one can continue with the ice accretion simulation. The droplet impingement in this thesis is calculated in the DROP3D module of FENSAP-ICE, which can determine the mass of water captured by the geometry and the impingement limits [86]. The module implements an Eulerian two-fluid model consisting of the Euler or Navier-Stokes equations for inviscid and viscous flows respectively, extended by the particle continuity and momentum equations [65, 76]. The mathematical model was introduced by Bourgault et al. [87] and it can be expressed as

$$\frac{\partial \alpha}{\partial t} + \nabla \cdot (\alpha u_d) = 0 \tag{3.10}$$

$$\frac{\partial u_d}{\partial t} + u_d \cdot \nabla u_d = \frac{c_{d\_droplet} Re_d}{24K} (u_a - u_d) + \left(1 - \frac{\rho}{\rho_w}\right) \frac{1}{Fr^2} g \tag{3.11}$$

in which the air velocity is presented as u_a and the droplet velocity is u_d. The water volume fraction is expressed as α and *K* stands for the droplet inertia. *Fr* and ρ_w depict the Froude number and the water density, respectively. In this module, the shape of the droplets is assumed to be spherical. This approximation is valid for applications in droplet Reynolds number Re_d below 500 [88]. The size of the droplets is uniform corresponding to the median volume diameter. An empirical relation based on the droplet Reynolds number is used to define the drag coefficient of the droplets $c_{d\_droplet}$ [76].

3.1.4 Ice Accretion and Water Runback

After obtaining the airflow and the droplet solution, the ice accretion can be calculated. The ice accretion module in FENSAP-ICE is ICE3D, which is a finite volume model. The ICE3D module calculates the ice accretion rate by using the friction force and heat flux information from FENSAP and the mass rate of droplet impingement obtained from the DROP3D module [67]. The model is based on a set of partial differential equations of conservation [89], which was derived from the Messinger model [90] and further adapted to calculate ice accretion and water runback. An illustration of the heat and mass transfer implemented in the ICE3D model is presented in Figure 3.2.

Determining the fluid film is an essential part of the ice accretion simulation. The water film velocity u_f is a function of the surface coordinates with the x-axis on the surface and the y-axis normal to the surface. It is known through observation that the film thickness in icing simulations is rarely greater than 10 μm [91]. Therefore, one can assume a linear velocity profile in the normal to surface direction [67]. The velocity at the wall is zero, thus giving the equation of the water film velocity as

$$u_f(x, y) = \frac{y}{\mu_w} \tau_{wall}(x, y) \tag{3.12}$$

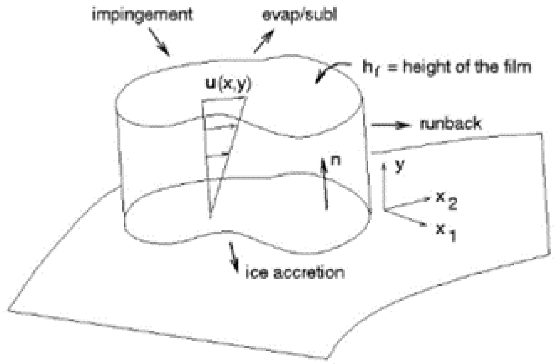

Figure 3.2: An illustration of the heat and mass transfer phenomena in the ICE3D module, from ANSYS FENSAP-ICE user manual [65].

with τ_{wall} being the shear stress from the air and μ_w describing the dynamic viscosity of water. The average velocity of the fluid film can be determined by integrating Equation 3.12 over the water film thickness h_f, which can be expressed as

$$\overline{u}_f(x,y) = \int_0^{h_f} \frac{y}{\mu_w} \tau_{wall}(x,y)\, dy = \frac{h_f}{2\mu_w} \tau_{wall}(x,y) \tag{3.13}$$

The equations lead to a system of partial differential equations, which are solved by the ICE3D module on all solid surfaces [65]. The first equation describes the conservation of mass

$$\rho_w \left[\frac{\partial h_f}{\partial t} + \nabla \left(\overline{u}_f h_f \right) \right] = u_\infty LWC\beta - \dot{m}_{evap} - \dot{m}_{ice} \tag{3.14}$$

where the terms on the right-hand side depict the mass transfer through water droplet impingement, which is a source, and also through evaporation and ice accretion, which is a sink. The second part of the partial differential system expresses the conservation of energy

$$\begin{aligned} \rho_w \left[\frac{\partial h_f C_w \tilde{T}}{\partial t} + \nabla \left(\overline{u}_f h_f C_w \tilde{T} \right) \right] &= \left[C_w \tilde{T}_{d,\infty} + \frac{\|u_d\|^2}{2} \right] \times u_\infty LWC\beta \\ &- 0.5 \left(L_{evap} + L_{subl} \right) \dot{m}_{evap} + \left(L_{fusion} - C_{ice}\tilde{T} \right) \dot{m}_{ice} \\ &+ \epsilon\delta \left(T_\infty^4 - T^4 \right) + \dot{Q}_h \end{aligned} \tag{3.15}$$

where the first three terms on the right-hand side represent the heat transfer obtained through impinging supercooled water droplets, evaporation, and ice accretion, respectively. The remaining terms express the radiative, convective, and one-dimensional conductive heat fluxes.

The ICE3D module is also capable of calculating the required anti-icing loads to prevent ice on the walls of the geometry at a specific icing condition. There are two available mass and thermal balance scenarios: running wet and fully evaporative. The running wet scenario calculates the heat flux necessary to maintain the water film at 0 °C so that no ice forms.

On the other hand, the fully evaporative scenario determines the minimum required anti-icing loads to evaporate all impinging water droplets. Consequently, the fully evaporative scenario demands higher heat flux values. However, with the running wet scenario, there is a chance the runback liquid water re-freezes in areas unprotected by the anti-icing system.

3.1.5 Multishot Simulation with Automatic Remeshing

In FENSAP-ICE, it is possible to divide the ice accretion simulation into multiple steps. This is shown to improve the quality of the ice shapes obtained [85]. There are two grid displacement algorithms implemented in FENSAP-ICE: OptiGrid and Fluent Meshing. A key difference between the two is that OptiGrid merely adapts the grid by displacing the existing nodes to fit the formed ice, while Fluent Meshing generates a new grid based on the ice shape. OptiGrid has the advantage of needing low computational power. However, the method is less appropriate for high ice accretion or complex geometries [65], which is often the case with glaze icing conditions. To generate a new grid, Fluent Meshing requires additional files to set up. These are depicted in Table 3.1. The ice shape is exported to FLUENT for remeshing and later imported back to FENSAP by using the custom_remeshing.jou file. The remeshing.jou file contains the commands required to calculate the new grid. The parameters of the grid generation are contained in the meshingSizes.scm file. Despite requiring higher calculation time, Fluent Meshing offers more stability and control of the new grid. The simulations in this thesis are done in a 10-shot multi-shot simulation with a custom Fluent Remeshing script.

Table 3.1: Additional files required for setting up the Fluent Remeshing procedure.

File Name	Description
custom_remeshing.jou	Interaction between FENSAP and FLUENT
remeshing.jou	Grid generation procedures
meshingSizes.jou	Parameter control for the grid generation

3.2 Verification and Validation Data

Verification and validation of CFD simulations intend to assess that the level of uncertainty and errors are within an acceptable range [92]. This step is necessary to determine the credibility of the simulation results. NASA defined verification as a process that examines if the computational models are accurately implemented and whether the codes are appropriate for analysis [93]. Verification of a calculation includes conducting a grid dependency study, which will be further described in Section 3.4. The validation process examines to which degree the simulation model agrees with physical reality [94]. It is only possible to validate models in ranges for which experimental data is available. This is a difficult challenge, especially for ice accretion studies since icing wind tunnel models need to match a lot more dimensionless quantities compared to conventional wind tunnel models [44]. The following subsections describe the ice accretion studies chosen as verification and validation data in this thesis.

3.2.1 AERTS Experimental Ice Shapes

The ice shapes obtained by Han, Palacios, and Smith [95] were used to verify and validate the ice accretion simulations in this thesis. The experiments were conducted in the adverse environment rotor test stand (AERTS) facility [96] at the Pennsylvania State University. The rotor icing test stand has a 10 ft hover stand built inside a climate chamber, where the icing condition parameters can be configured. The climate chamber can reach a temperature as low as −20 °C. The geometry used in the study is an untampered, non-swept, and no-twist blade with a 10.5-inch chord length and a NACA 0012 cross-sectional profile. This blade geometry was chosen by the authors to better represent a full-scale helicopter blade and to allow a similar shape as the blades used at the NASA Glenn Icing Research Tunnel. The experimentally obtained ice shapes were captured using a 3D laser scanning method. The testing conditions are presented in Table 3.2. The test runs chosen for the verification and validation data are AERTS cases number 14 and 29 to simulate rime and glaze ice conditions, respectively. The obtained ice shapes are shown in Figure 3.3.

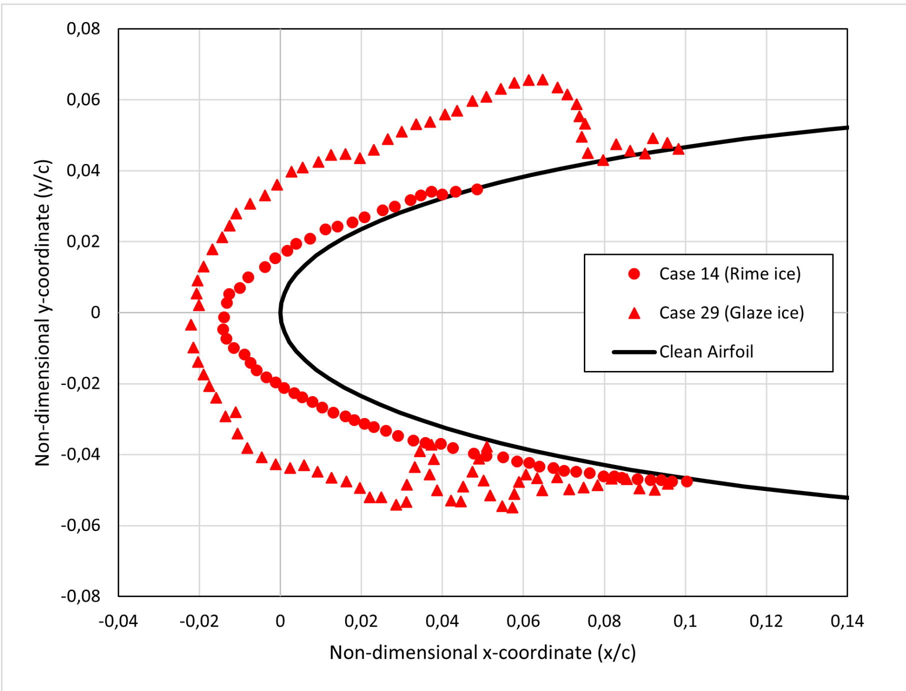

Figure 3.3: Experimental ice shapes from a study by Han et al. [95] chosen as verification and validation data.

Table 3.2: Selected testing conditions from the AERTS ice accretion experiments obtained from a study by Han et al. [95].

Case	Temp [°C]	V [m/s]	MVD [μm]	LWC [g/m^3]	Time [min]	AOA [°]
14	-15.4	56.2	28	0.44	4.1	3.5
29	-5.7	67.1	26.2	0.86	4.0	0

3.2.2 VTT IWT Experimental Ice Shapes

The numerical ice shapes calculated in this thesis were also compared against the ice shapes obtained in an experimental campaign by the UAV Icing Lab [97]. The experiments were conducted at the VTT Technical Research Center icing wind tunnel [98] in Helsinki, Finland. The open loop wind tunnel has an enclosed test section, which is placed within a cold chamber. The facility can produce wind speeds up to 50 m/s and achieve temperatures as low as $-25°C$. Water droplets are introduced with spray nozzles that inject liquid water into the airflow. The liquid water content and the median volume diameter can be set between 0.1 g/m^3 to 1 g/m^3 and 12 μm to 30 μm respectively [98]. The ice accretion experiments were conducted on a 15-inch Mejzlik rotor. The test rotor was mounted on a Series 1580 Test Stand by Tyto Robotics with torque and thrust measurement capabilities and equipped with an optical RPM probe. The ice shapes were acquired using photogrammetry using the software Metashape from Agisoft [99]. The test runs chosen as comparison data are run number 116 to represent glaze ice conditions and run number 177 for rime ice conditions. The VTT testing conditions are presented in Table 3.3.

Table 3.3: Selected testing conditions from the VTT IWT ice accretion experiments obtained from a test campaign by the UAV Icing Lab at NTNU [97].

Case	Temp. [°C]	MVD [μm]	LWC [g/m^3]	Time [s]
Run 116	-5	24.3	0.41	120
Run 173	-10	24.3	0.41	60
Run 177	-15	24.3	0.41	60

3.3 Geometries and Grid Setup

Three different geometries were used in this study. The verification and validation of the simulations were done on a NACA 0012 airfoil. The ice accretion simulations were performed on a 15-inch rotor to represent eVTOL UAVs and an 80-inch rotor to approximate a UAM eVTOL aircraft. The CAD models of the rotors were provided by the Mejzlik [100]. The

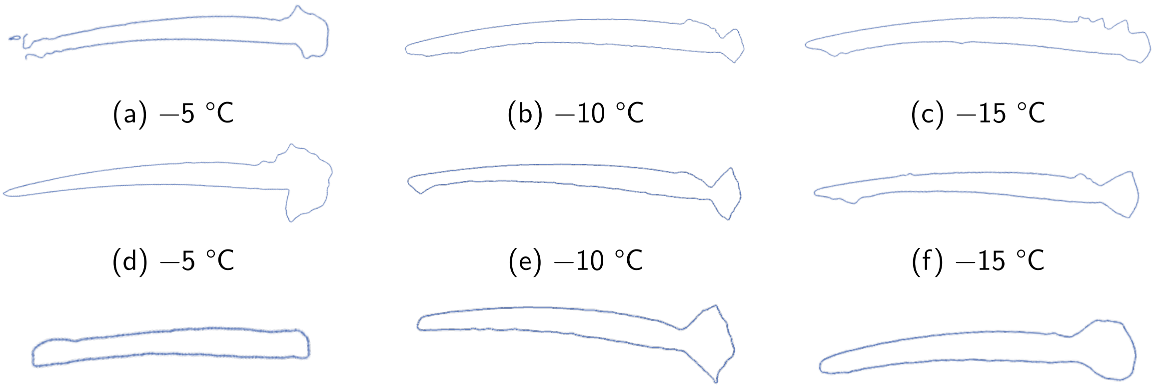

(a) −5 °C (b) −10 °C (c) −15 °C

(d) −5 °C (e) −10 °C (f) −15 °C

(g) −5 °C (h) −10 °C (i) −15 °C

Figure 3.4: Comparison of the VTT IWT ice shapes from the UAV Icing Lab at NTNU [97]. The subfigures in the first row depict the ice shapes at 50% blade radius, while the second and third illustrate the 75% and 95% respectively. The ice shapes in the left column display the experimental results from run 116, the middle column from run 173, and the right column from run 177.

NACA 0012 airfoil was obtained from a database provided by Selig [101]. The rotor sections were created using the CAD software Siemens NX [102] and the mesh is generated using Pointwise [103] version 18.6. The ice accretion simulations in this thesis start with a two-dimensional approach then followed by a simulation in 3D.

The 2D mesh is generated as an O-type grid with a far-field size of 20 times the airfoil chord length and an unstructured resolution. The airfoil geometry is split at approximately 20% from the leading edge to differentiate the parts mostly impacted by ice and to resolve them with more detail than the rest of the airfoil. The initial cell height of the grids is set between 1-5E−06 m depending on the airfoil size and a growth rate of 1.1 to achieve a dimensionless wall distance of y+<1 for the first point. This step is necessary to ensure that the boundary layer and the viscous layer are well resolved, to correctly calculate the friction coefficients. Furthermore, the T-Rex function from Pointwise is applied to generate anisotropic layers at the boundary. The function is especially suitable for unstructured domains on geometries with high curvature [104]. The cell type is set to triangles and quads to enable anisotropic layers consisting of triangular and quadrilateral cells. Finally, the grid is extruded by 0.2 times the airfoil chord length in a spanwise direction. The reference area, which FENSAP-ICE requires to calculate the lift and drag forces, is obtained by multiplying the reference area with the chord length.

3.3.1 NACA 0012

The NACA 0012 airfoil is chosen to mimic the geometry used in the validation data [95]. The geometry has a cross-sectional chord length of 0.267 m and it is neither swept, tapered nor twisted. The original NACA 0012 airfoil was obtained from a database by Selig [101]. For this study, the airfoil's trailing edge is modified using XFOIL [105] to get a blunt trailing edge with a 1 mm gap. This is done to achieve a more realistic geometry. A comparison of the original and modified airfoil is shown in Figure 3.5.

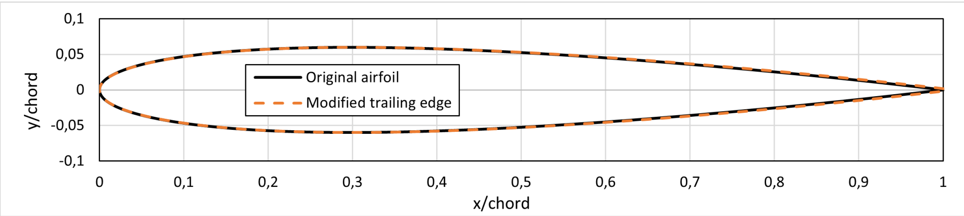

Figure 3.5: An illustration of the original and the modified NACA 0012 airfoil.

In addition to the initial mesh, a finer and coarser mesh is also generated for the NACA 0012 case. This is done to investigate the grid dependency, which will be described further in Subsection 3.4. The additional meshes are created with a refinement ratio of $r = \sqrt{2}$. The initial cell height for all grids is set to 5E−06 m. The far-field size and the extrusion rate remain the same, while the growth rate is adapted. Figure 3.6 presents the NACA 0012 initial grid and a description of the grid setup is shown in Table 3.4.

Table 3.4: Mesh features of the NACA 0012 ice accretion grid.

Mesh feature	Finer mesh	Initial mesh	Coarser mesh
Points on upper and lower side	255	180	130
Leading edge spacing [mm]	0.28	0.40	0.56
Trailing edge spacing [mm]	0.65	0.80	1.13
Points on far field inlet	850	600	425

3.3.2 Mejzlik 15x5 inch Rotor

The Mejzlik 15-inch rotor was chosen to represent the rotor size of an eVTOL UAV. The two-bladed rotor has a 15-inch diameter and a 5-inch pitch at 75% blade radius. The CAD model of the rotor can be seen in Figure 3.7. It is a lightweight rotor designed for multicopter use. The rotor can spin up to 12000 RPM before the blade tips reach 0.7 Mach. The rotor performance as given by Mejzlik [106] can be found in Figure 3.8. It is the same rotor used in the VTT validation data.

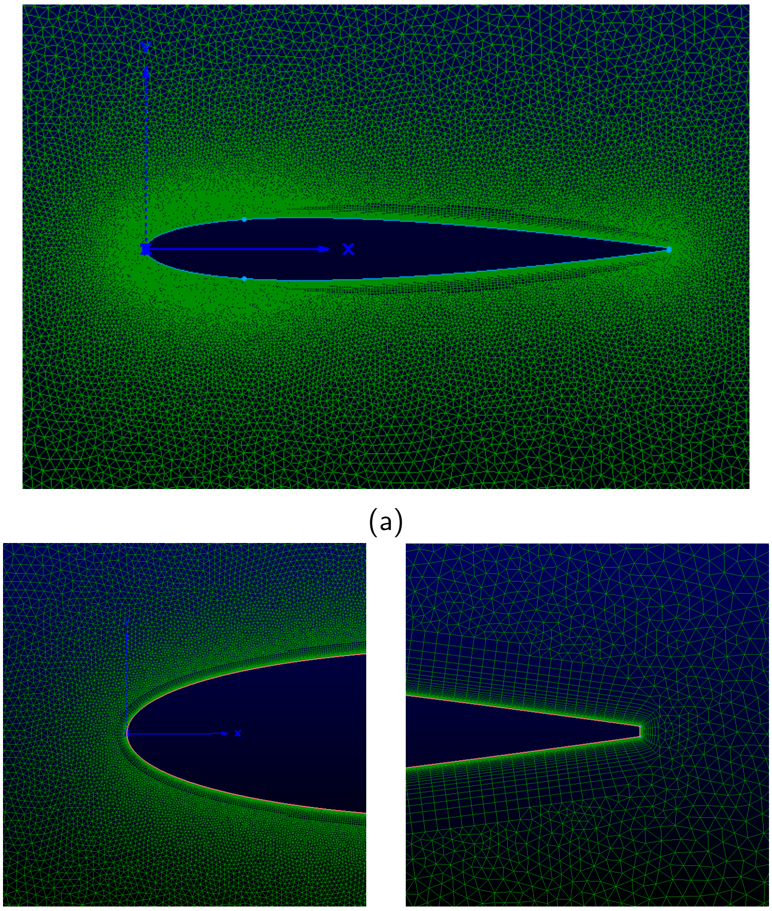

(a)

(b) (c)

Figure 3.6: An illustration of the NACA 0012 initial mesh (a) and the mesh focused on the leading edge (b) and trailing edge (c).

For the 2D ice accretion simulations, the cross sections of the blade were taken in three different positions. A description of the rotor sections including chord length and blade twist is presented in Table 3.5. To improve the mesh quality, the trailing edge of the sections has been modified to a blunt trailing edge in Pointwise. Figure 3.9 illustrates the distribution of chord length versus the blade twist angle of the rotor. The grid generation generally follows the same workflow as with the NACA 0012. However, some differences had to be applied to account for the smaller, thinner airfoil cross sections. The differences to the initial mesh are presented in Table 3.6. The 3D mesh of the 15-inch rotor was created with a cylindrical far field with a distance of 10 times the blade radius to the rear and 5 times the blade radius to the front and sides. The blade leading edge is set with a constant 1024 points and the trailing edge has 1000 points on both ends. With a decay value of 0.5 and an initial cell height of 1E−06, the 3D mesh consisted of 6.5 million cells. A slice of the mesh is presented in Figure 3.10.

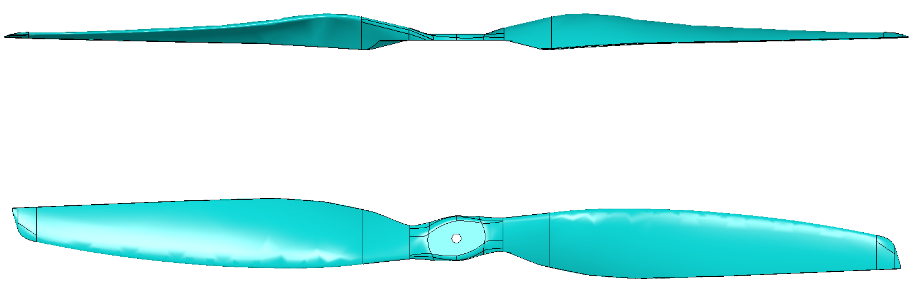

Figure 3.7: CAD model of the 15-inch Mejzlik rotor.

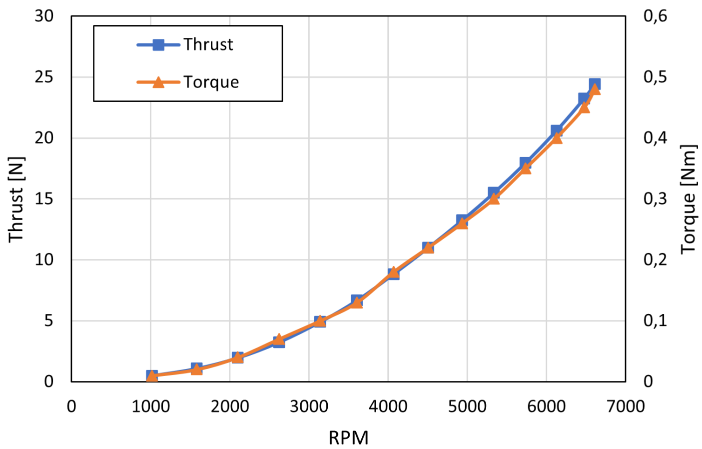

Figure 3.8: The Mejzlik 15-inch rotor thrust and torque performance, data provided by Mejzlik [106].

3.3.3 Mejzlik 80x28 inch Rotor

The second rotor is an 80-inch rotor from the same manufacturer. This dimension is chosen to approximate the size of rotors utilized in UAM eVTOL aircraft. The rotor has a diameter of 80 inches and a 28-inch pitch at a 75% radius. An illustration of the rotor can be seen in Figure 3.11. The rotor is designed for high-performance multicopters and spins counterclockwise. The maximum rotation rate for the blade tips to remain subsonic is 2300 RPM. The rotor performance as given by the manufacturer [106] can be found in Figure 3.12.

Similar to the 15-inch rotor, cross sections of the 80-inch rotor blade were taken in three positions: at 50%, 75%, and 95% radial position. The cross-sections were obtained using Siemens NX and exported to Pointwise for meshing. Table 3.7 presents a full description of the rotor sections. Due to its larger size, some meshing features were also adapted and thus differ from the verified mesh generation workflow. The upper and lower side of the airfoil was generated using 250 points, while the far field was defined with 800 points. The cell initial height for all 80-inch rotor sections is 2.5E−06 m. The leading edge and trailing edge spacing

Table 3.5: Airfoil sections of the 15-inch rotor used for the 2D simulations.

Blade radius [%]	Chord length [m]	Twist angle [°]
50	0.02994	12.91
75	0.02308	8.77
95	0.01475	6.30

Table 3.6: Varying mesh features of the 15-inch rotor.

Mesh feature	50%	75%	95%
Leading edge spacing [mm]	0.05	0.04	0.02
Trailing edge spacing [mm]	0.10	0.08	0.04
Initial cell height [m]	2E−06	2E−06	1E−06

of the airfoil at 50% and 75% radial positions are 0.15 mm and 0.30 mm, respectively. The outer airfoil section at 95% of the blade radius has a finer leading edge spacing of 0.1 mm and a trailing edge spacing of 0.2 mm to better resolve the geometry. Figure 3.13 illustrates the distribution of chord length versus the blade twist angle of the rotor. The 3D mesh of the 80-inch rotor was created with a sphere far-field with a sphere radius of 5 times the blade radius. The blade leading edge is set with a constant 1200 points and the trailing edge has 1000 points on both ends. With a decay value of 0.9 and an initial cell height of 1E−05 m, the 3D mesh consisted of 12.9 million cells. A slice of the mesh is presented in Figure 3.14.

Table 3.7: Airfoil sections of the 80-inch rotor used for the 2D simulations.

Blade radius [%]	Chord length [m]	Twist angle [°]
50	0.1603	12.97
75	0.1236	8.82
95	0.0791	6.00

3.4 Grid Dependency Study

The discretization of the flow field and geometry is an important step in any CFD simulation. Seeing that the governing equations are only calculated at the nodes, the mesh quality heavily influences the results obtained. The spatial resolution of the flow field, boundary layer, and adequate resolution of the geometry are some aspects that need to be considered. Generally, a fine mesh would deliver more accurate results. However, this would translate to higher computational power and time consumption. A mesh may be coarser in areas of less interest to save resources. A good balance between a fine resolution and acceptable computational

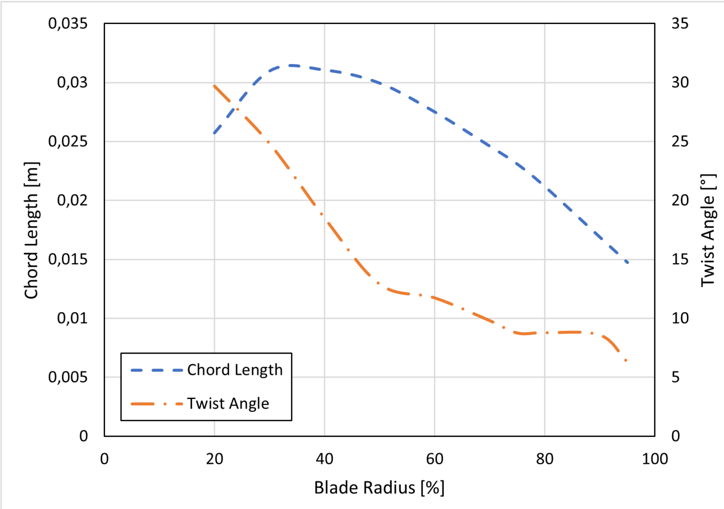

Figure 3.9: The distribution of the blade twist angle and chord length along the blade radius of the 15-inch rotor.

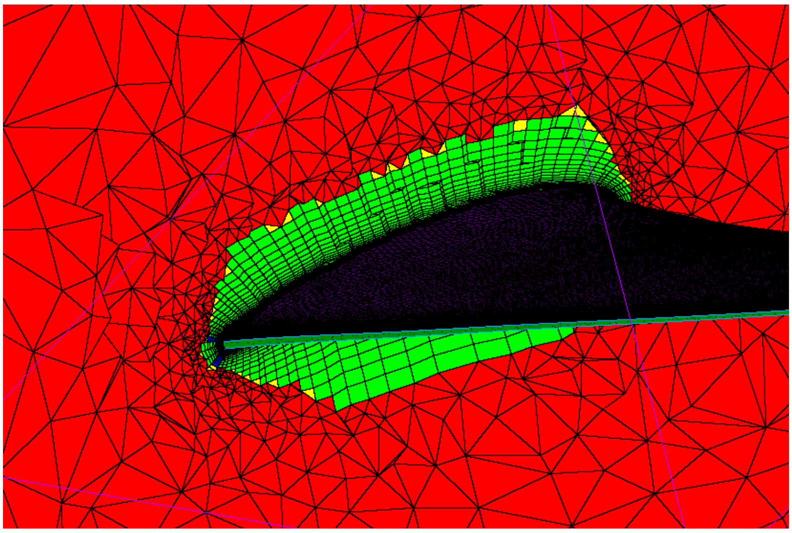

Figure 3.10: Slice of the 15-inch 3D mesh at 75% blade radial position.

resources is often sought after. Therefore, it is important to examine the spatial convergence to verify that the simulation results are independent of the grid resolution. In his book, Roache [107] presented an extensive explanation of the grid convergence study. A summarized version is offered by the NPARC Alliance [108].

To begin, a minimum of three meshes with varying fineness and a constant refinement ratio r are generated and simulated. The grid refinement ratio should not be less than 1.1 [108] to differentiate the discretization error from other computational errors. A parameter is chosen to investigate the grid convergence and plotted against the grid spacing h. Should the results show a monotonous trend, the theoretical true value at zero grid spacing can be calculated using the Richardson extrapolation [109, 110]. This is owed to the fact, that the Richardson extrapolation is based on a Taylor series and therefore is invalid in regions of discontinuity.

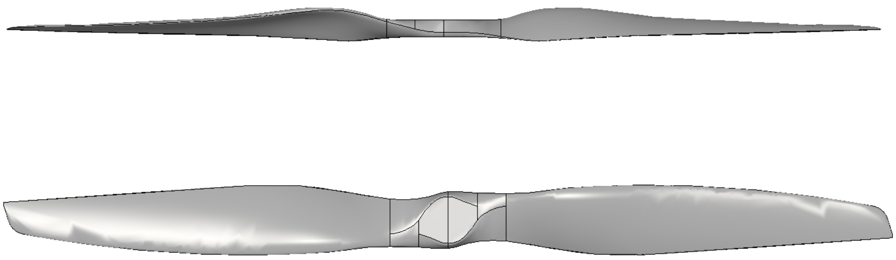

Figure 3.11: CAD model of the 80-inch Mejzlik rotor.

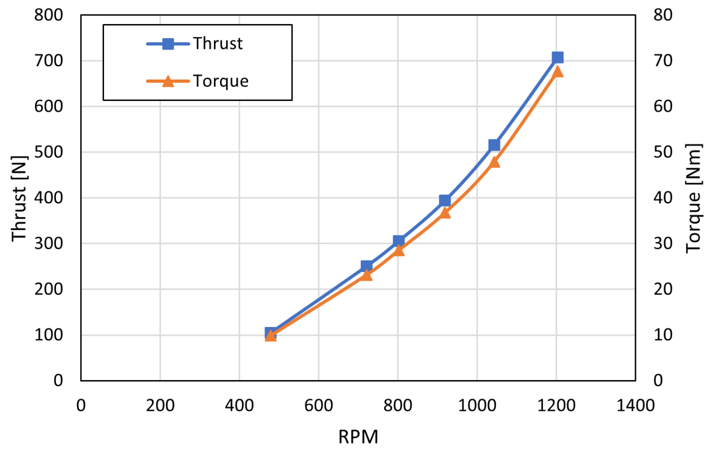

Figure 3.12: The Mejzlik 80-inch thrust and torque performance, data provided by Mejzlik [106].

To do that, one should first calculate the order of grid convergence *p*, which is the difference between the exact and the discreet solution. A direct, simplified evaluation of *p* can be calculated using three solutions of a simulation *f* with a constant grid refinement ratio *r* and is expressed as

$$p = \frac{\ln\left(\frac{f_3 - f_2}{f_2 - f_1}\right)}{\ln(r)} \tag{3.16}$$

The idea behind the Richardson extrapolation is to obtain an estimate of a continuum value using a series of discrete values. It can be depicted as

$$f_{h=0} \cong f_1 + \frac{f_1 - f_2}{r^p - 1} \tag{3.17}$$

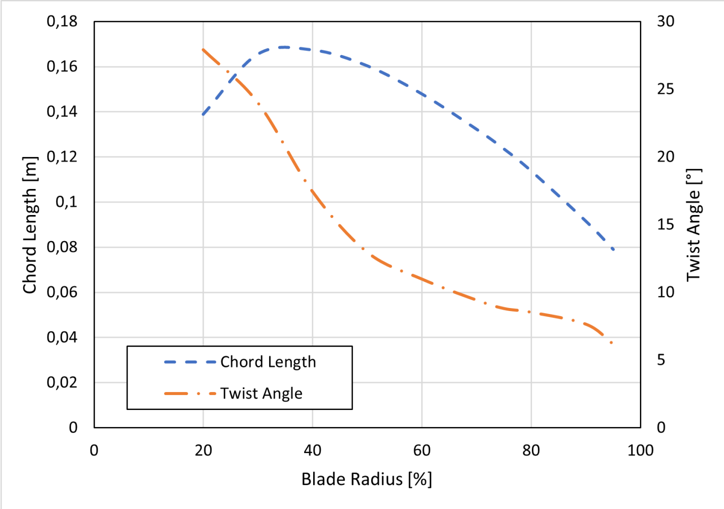

Figure 3.13: The distribution of the blade twist angle and chord length along the blade radius of the 80-inch rotor.

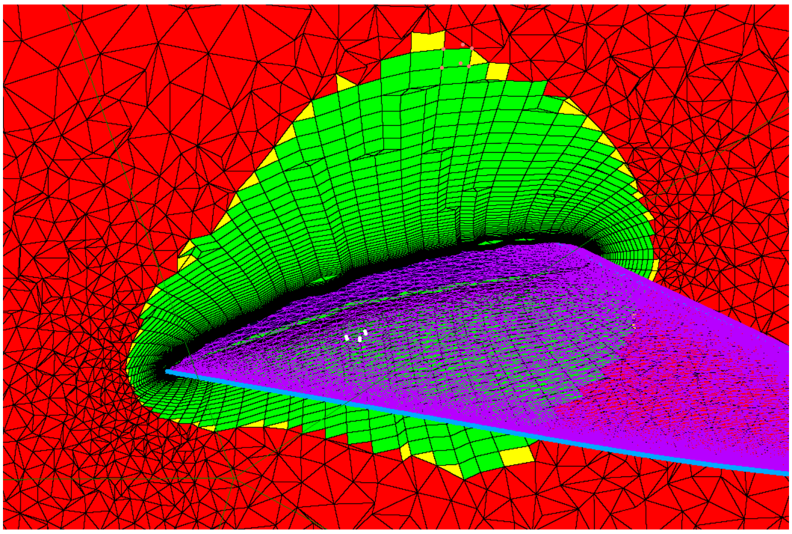

Figure 3.14: Slice of the 80-inch 3D mesh at 75% blade radial position.

for methods of p-th order. The next step would be to calculate the grid convergence index (GCI). This methodology was provided by Roache [107] to enable a standardized presentation of grid refinement studies. The GCI measures the error between the computed value and the asymptotic numerical value. It indicates how a simulated value would differ with further mesh refinement. The GCI of the fine and coarse mesh can be calculated with

$$GCI_{fine} = \frac{F_s|\epsilon|r^p}{(r^p - 1)} \tag{3.18}$$

$$GCI_{coarse} = \frac{F_s|\epsilon|r^p}{(r^p - 1)} \tag{3.19}$$

Roache recommends the use of a safety factor F_s of 3.0 for a comparison of two grids and 1.25 for studies with three or more meshes. Finally, the asymptotic range of convergence can be observed by applying the GCI to

$$\frac{GCI_{fine}}{r^p \times GCI_{coarse}} \approx 1 \tag{3.20}$$

If the left-hand side of Equation 3.20 is approximately equal to 1, the simulation solutions lie within the asymptotic range of convergence and therefore approach a converged solution.

3.5 Atmospheric Icing Conditions

The Federal Aviation Administration described in Appendix C of the Code of Federal Regulations Title 14 Part 25 [18] various envelopes for determining values used in in-flight icing studies. The continuous maximum icing defines the icing conditions in a stratiform cloud with a horizontal extend of 17.4 nautical miles and for flight altitudes between sea level and 22.000 ft. The intermittent maximum icing characterizes an envelope in a cumuliform cloud with a horizontal extend of 2.6 nautical miles and it is valid for flight altitudes between 4.000 to 22.000 ft.

Table 3.8: Icing conditions for the 15-inch rotor simulations based on the VTT IWT experimental test runs.

Case	Temp. [°C]	MVD [μm]	LWC [g/m^3]	Time [s]
Glaze	-5	24.3	0.41	120
Mixed	-10	24.3	0.41	60
Rime	-15	24.3	0.41	60

Table 3.9: Icing conditions for the 80-inch rotor simulations.

Case	Temp. [°C]	MVD [μm]	LWC [g/m^3]	Time [s]
Glaze	-2	20	0.595	300
Mixed	-5	20	0.531	300
Rime	-15	20	0.319	300

The icing conditions used for the 15-inch rotor simulations are presented in Table 3.8. The values are chosen to replicate the icing conditions during the VTT icing wind tunnel experiments. A short icing time for small rotors and propellers is chosen to consider the ice build-up before ice shedding occurs, which depends on temperature and the centrifugal forces acting on the blade [45]. Table 3.9 describes the icing conditions for the 80-inch rotor simulations. In the Advisory Circular No 20-73A [41], the Federal Aviation Administration suggests the use of the Langmuir-D [111] droplet distribution for MVDs below 50 μm [65].

Despite this, the rotor simulations were conducted using a monodisperse distribution due to computational time restrictions. An MVD of 20 μm and a temperature of -2 °C were chosen as it is the worst-case scenario for icing on the wing of a UAV [35]. A simulation at -5 °C is conducted to predict how the ice accretes in mixed ice conditions. Previous studies on a UAV propeller [45] show that lower temperatures tend to have larger performance degradation. Therefore, the rotor is also simulated at a temperature of -15 °C. The icing duration was decided based on an estimation of a UAM aircraft mission profile. To be able to operate in urban areas, a UAM aircraft is expected to be able to hover, take off and land vertically. Possible UAM mission profiles are described in studies by Johnson and Silva [112], Kadhiresan and Duffy [113], and Hill et al. [57], which is approximately illustrated in Figure 3.15. It is important to note, that the transition mechanism and duration of a UAM aircraft depend highly on the aircraft's configuration. To simplify the simulation, the transition and climb phase is omitted in this thesis and the UAM eVTOL is assumed to climb vertically from ground level to its cruising altitude. An icing time of 300 seconds was decided to illustrate a fully vertical take-off to a cruising altitude of 1500 ft with a climb rate of 1.5 m/s.

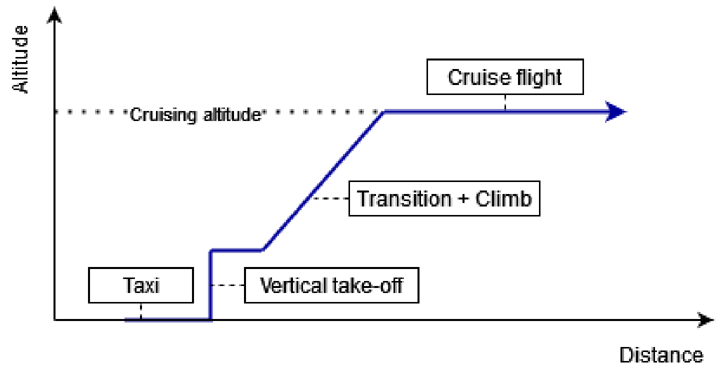

Figure 3.15: An illustration of a generic UAM aircraft take-off profile based on studies by Johnson and Silva [112], Kadhiresan and Duffy [113], and Hill et al. [57].

3.6 Flow Conditions

Air density is influenced by the temperature and pressure of the air. For this reason, the air is categorized as a compressible fluid. A compressible flow treats the flow as a continuum, instead of tracking the individual molecules. This assumption is valid for most gas dynamic problems except for low-density fluids [69]. A consequence of compressibility is the maximum achievable speed where pressure changes propagate through a medium. This is called the speed of sound a and it is expressed as

$$a = \sqrt{\kappa RT} \tag{3.21}$$

where k represents the isotropic coefficient, R is the universal gas constant and T stands for temperature. The ratio of flow velocity corresponding to a boundary to the local speed of sound is called the Mach number, which is described as

$$Ma = \frac{v}{a} \tag{3.22}$$

The Mach number is commonly used to determine the compressibility of a flow since a flow with a Mach number less than 0.3 can be treated as incompressible [114]. Furthermore, the different Mach number regimes also have different flow characteristics. Propeller-driven and turbofan aircraft operate at the subsonic regime, where the airflow over the aircraft is less than 1. For aircraft with rotating lifting surfaces, it is important to mind the local Mach number at the blade tips as it should ideally not exceed 0.7. The rotors studied in this thesis rotate with a rate of 5000 RPM for the 15-inch and 1500 RPM for the 80-inch, which translates to a tangential velocity at the blade tip of approximately 100 m/s and 160 m/s for the small and large rotors, respectively. The rotation rate of the small rotor was chosen to match the setup used in the VTT IWT icing experiments, while the rotation rate of the large rotor was chosen so the rotor can generate approximately 900 N of thrust and the blade tips remain below Mach 0.7.

Another aspect considered when determining the flow conditions is the flight behavior. An eVTOL aircraft is attractive for the UAM industry as it offers a range of maneuverability such as vertical take-off and landing, hover, sideways flight, etc. The simulations in this thesis assume the rotors operate in hover with moderate wind. Hover flight was chosen to eliminate the effects of the airspeed component occurring in horizontal flight. An additional vertical wind speed of 6 m/s, which is classified as a moderate wind in the Beaufort scale [115], is additionally implemented to simulate real-life conditions. The rotor flapping, coning, and ground effects are not taken into consideration in this thesis.

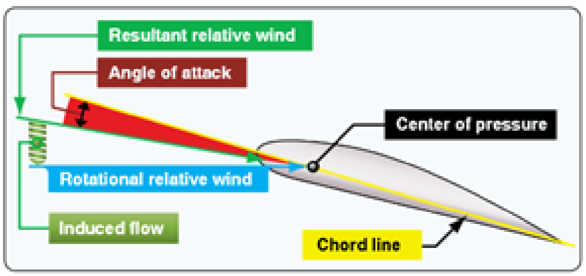

Figure 3.16: Airflow components acting on a rotor blade airfoil, based on the FAA helicopter handbook [116].

The airflow components acting on a blade airfoil are illustrated in Figure 3.16. The rotational relative wind is obtained by adding the local tangential velocity due to rotation and the wind speed. The induced flow is the downward displacement of air caused by the horizontal motion of a moving object [116]. Rotor blades rotate on the same path and thus move through the same point in succession. This pushes the still air into a downward motion. Induced flow is greatest at hover flight conditions without wind and it effectively lowers the local angle of attack [116]. The induced flow velocity can be estimated by applying the momentum theory. Assuming a steady flow, uniform thrust, and hover, the induced velocity can be calculated as

$$v_1 = \sqrt{\frac{T}{2\rho A}}. \tag{3.23}$$

Equation 3.23 only serves as a quick estimation as the assumptions taken are not satisfied by real-life rotors. Houghton et al. [117] provided a detailed derivation of the induced velocity equation. The thrust values were provided by the rotor manufacturer.

The resultant relative wind at hover is a combination of the rotational relative wind and the influence of induced flow. At horizontal flight, an airspeed component is introduced and further modifies the resultant relative wind. Depending on where the blade is, either advancing or retracting concerning the aircraft movement, the airspeed component is added or subtracted. This is called the dissymmetry of lift [116]. A similar condition is also present when the aircraft is at hover with headwind or crosswind. A summary of the velocity components used in this thesis is presented in Table 3.10.

Considering the variable angle of attack depending on blade location and airspeed [116], the air velocity in the 2D simulations within this thesis was set to its local resultant relative wind without a velocity angle since the angle of attack is within the blade twist angle. The local angle of attack can be determined by subtracting the angle between the resultant relative wind and the rotor disk from the blade twist angle and is presented in Table 3.11. The local blade twist angles can be found in Table 3.5 for the 15-inch rotor and in Table 3.7 for the 80-inch rotor. There are several published works available presenting studies and suggestions on the angle of attack determination of rotor blades, for example, the study by Shen et al. [118]. However, the exact calculation of the angle of attack is not within the scope of this thesis. Therefore, an approximation was done instead.

Table 3.10: Velocity components of the flow applied to the 2D simulations within this thesis.

Rotor	**15 inch**			**80 inch**		
Blade radius [%]	50	75	95	50	75	95
Local tangential velocity [m/s]	49.87	74.81	94.76	79.79	119.69	151.07
Rotational relative wind [m/s]	55.87	80.81	100.75	85.79	125.69	157.61
Induced flow velocity [m/s]	13.77	9.18	7.24	21.34	14.23	11.23
Resultant relative wind [m/s]	57.54	81.32	101.01	88.41	126.49	158.01

Table 3.11: Local angle of attack and the angle between the relative wind and the rotor disk for all studied airfoil sections.

Rotor	**15-inch**			**80-inch**		
Blade radius [%]	50	75	95	50	75	95
Angle of incidence [°]	13.84	6.48	4.11	13.97	6.45	4.07
Angle of attack [°]	−0.93	2.28	2.18	−1.00	2.36	1.92

4 Results

In this chapter, the results of the simulations conducted in this thesis are presented. The first section covers the verification and validation of the simulation model. The section starts with the grid dependency study to investigate whether the simulation results are reliant on the mesh resolution. It is followed by a parameter study to observe the effects of different parameter setups, and finally, the obtained ice accretion is validated against an experimental data set. The following sections present the results of the ice accretion, performance degradation, and anti-icing load simulations, respectively.

4.1 Verification and Validation of the Simulation Model

Before performing the CFD simulations, the models have to be verified and the parameters set up. This step is done with care as the quality of the obtained numerical results can be heavily influenced by the mesh resolution and the setup. After investigating the grid convergence and defining the parameter setup, the model is validated against experimental results. It is important to note, that the experiments performed by Han et. al [95] were conducted at a higher Reynolds number regime than the planned rotor simulations. This leads to incorrect modeling of the boundary layer. However, due to limited available experimental data, the work of Han et. al [95] was still chosen to validate the simulation results. The simulation setup established in this subsection will be used to conduct the ice accretion simulations on the small and large rotor sections.

4.1.1 Grid Dependency Study

Three separate grids with a constant refinement ratio of $r = \sqrt{2}$ were generated for the grid dependency study. The features of all three grids are presented in Table 3.4. The chord length of the airfoil is set to 0.266 m and the icing conditions follow the parameters used in the glaze and rime ice experiments by Han et. al [95]. A simulation is run for each grid resolution and both icing conditions. The lift and drag coefficient were chosen to investigate the grid convergence and it is plotted against the dimensionless grid spacing h in Figure 4.1 for the rime ice case and in Figure 4.2 for the glaze ice case. Except for the lift coefficient in the glaze ice case, the lift and drag coefficients present a monotonous trend. However, the gradients of the graph in the rime ice case go towards infinity. Therefore, a Richardson extrapolation can only be performed on the coefficients of the glaze ice case. Utilizing the methodology in Section 3.4, the order of grid convergence was calculated and then applied to the Richardson extrapolation equation. As shown in Figure 4.2b, the hypothetical exact solution is shown to converge. If we further calculate the grid convergence index (GCI) and the asymptotic range of convergence, it can be seen in Table 4.1 that the error band is narrow. The CGI value indicates the error between the grids [107]. An asymptotic range of approximately one implies that the grids are sufficiently refined [108], which is what the glaze ice drag coefficient calculation results in this grid dependency study suggest.

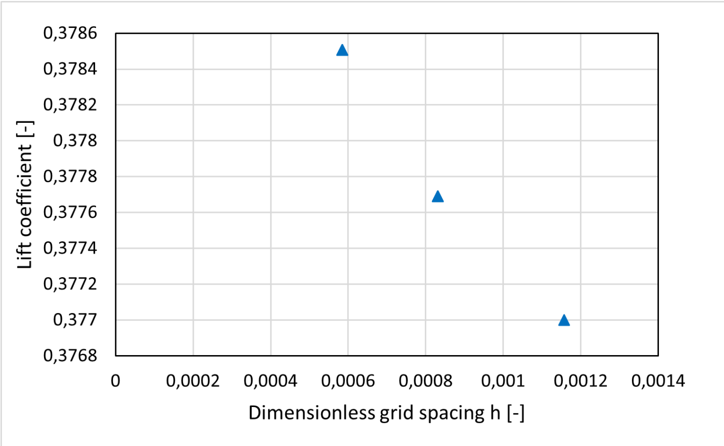

(a)

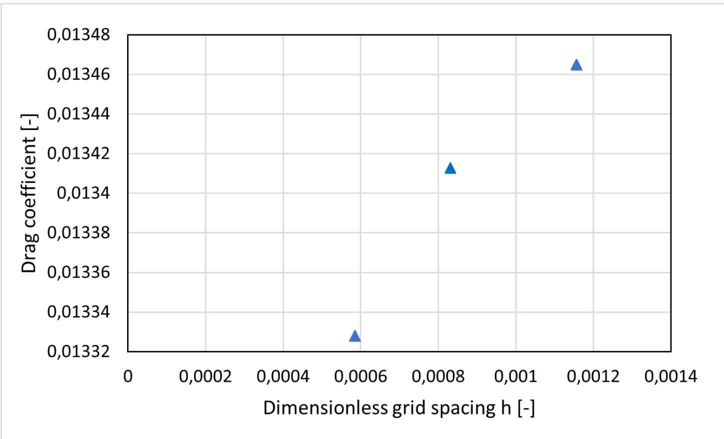

(b)

Figure 4.1: Lift (a) and drag (b) coefficients of the rime ice simulations for the grid dependency study.

The calculated lift coefficient of the glaze ice case, as illustrated in Figure 4.1a, shows discontinuity with the initial mesh calculating a lift coefficient of −0.7164E-04 while the fine and coarse mesh deliver a positive lift coefficient of −1.201E04 and −1.124E04 respectively. However, it is important to note that the studied NACA 0012 airfoil is symmetrical. In the glaze ice case, the simulation is run at 0° angle of attack, which in theory produces no lift [69]. With the simulated values being ten to the minus four power, the lift coefficient of the NACA 0012 in the glaze icing condition is virtually zero, thus in line with the theory. If we look at the lift coefficients of the rime ice case, it can be seen that the solutions lie within 0.18% – 0.22%

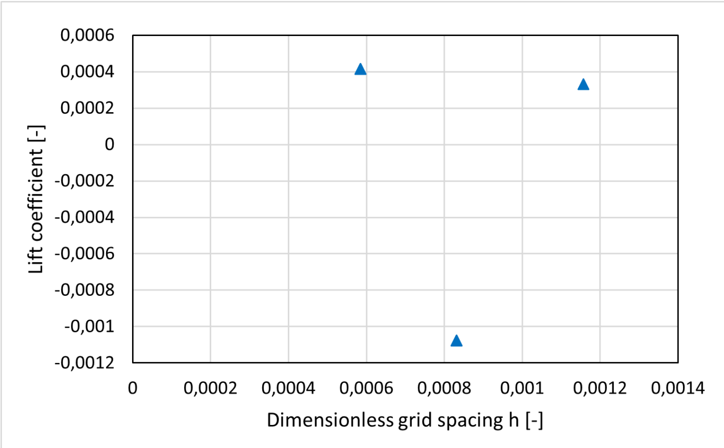

(a)

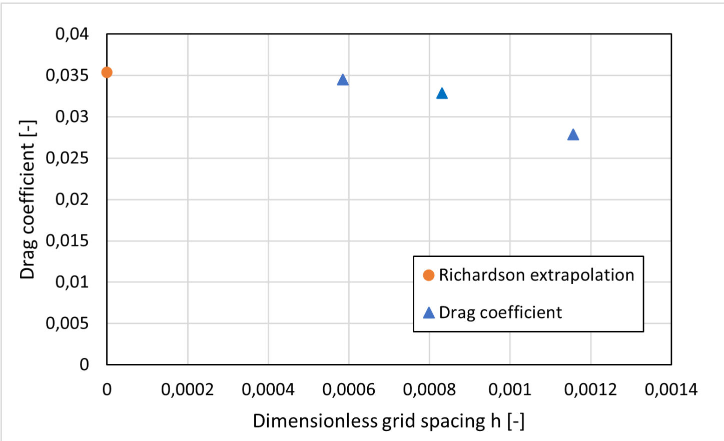

(b)

Figure 4.2: Lift (a) and drag (b) coefficients of the glaze ice simulations for the grid dependency study.

from each other, while the drag coefficients are situated between 0.39% – 0.64%. Since the deviations between the results are minor, it is assumed that the effects of grid dependency are minimum and can be neglected for all meshes. The initial mesh setup is decided to generate the grids of the rotor sections.

Table 4.1: CGI values and asymptotic range of convergence of the drag coefficient for the glaze ice case.

Parameter	
CGI coarse	9.411%
CGI fine	2.977%
Asymptotic range	1.0502

4.1.2 Numerical Parameter Study

After investigating the grid convergence, the effects of the various parameters are observed in this subsection. This is done to figure out the optimal setup for achieving realistic ice shapes numerically. The simulation runs were done with the NACA 0012 initial mesh and a selected number of AERTS case icing conditions. For more details, please refer to Table 3.4 and 3.2. The simulation model is set fully turbulence as it is assumed that the boundary layer transition would happen at the leading edge due to ice surface roughness. The droplet distribution is set to monodisperse with LWC and MVD values depending on the icing condition. All simulations were conducted using the Spalart-Allmaras turbulence model.

First, the effect of the multishot simulation is studied. In a multishot simulation, the total icing time is divided into smaller durations and the airflow and droplet distribution are calculated again for every step [65]. The idea behind this is to take the changes in the geometry due to ice accretion into account [85], thus aiming for more realistic ice shapes. A multishot simulation consisting of 10 steps was performed on the NACA 0012. The results are plotted against a single shot simulation as presented in Figure 4.3. The rime ice case shows small differences. The multishot simulation is shown to have a more streamlined shape, while the total ice mass remains similar. A greater variety of ice shapes is observed in the glaze ice case with the multishot simulation delivering more details compared to the mainly rounded shape of the single shot simulation.

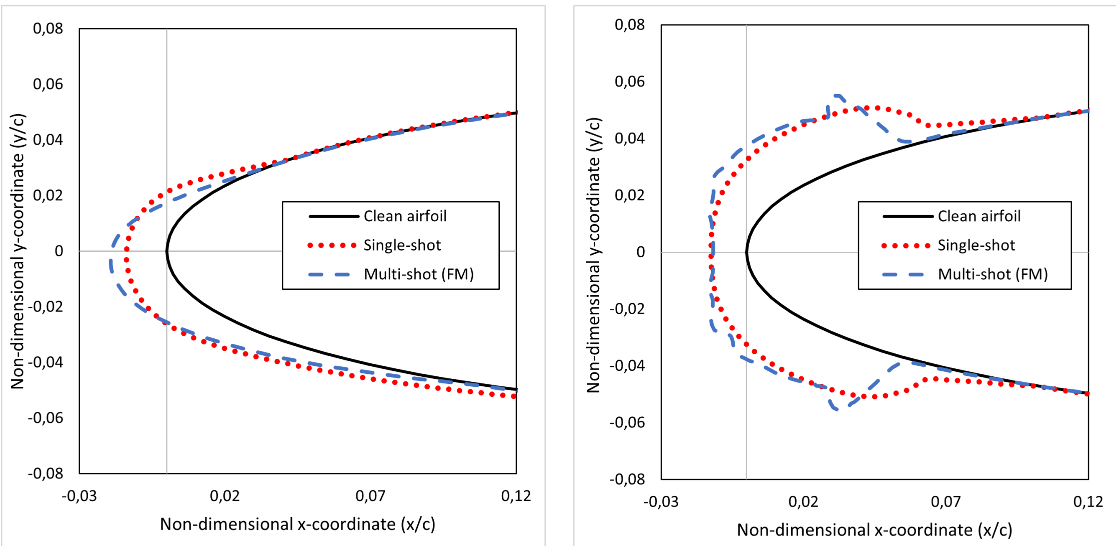

(a) (b)

Figure 4.3: A comparison of the results from a single shot and multi-shot simulation for the rime (a) and glaze (b) ice case.

ANSYS implemented two different automatic remeshing algorithms within the FENSAP-ICE module, namely OptiGrid and Fluent Meshing. OptiGrid is a mesh adaptation and CAD reconstruction software, which can be used for automatic remeshing between the icing simulation shots. Its mesh adaptation strategies include node displacement, refinement, and coarsening to reduce error as well as edge swapping to optimize the grid orientation and alignment [65]. It is important to note that OptiGrid does not change the grid topology but instead displaces already existing nodes. This saves computational time but comes with a limitation, especially when applied to complex ice shapes. Automatic remeshing using the Fensap Meshing module allows the user to bypass this limitation since Fensap creates a new grid based on the accumulated ice. This method offers more control options for the mesh generation and it is more suited for complex ice shapes [65].

The simulation model was run using both automatic remeshing algorithms and the results are compared in Figure 4.4. In the rime ice case, the ice shapes are practically identical. The remeshing sequence using the OptiGrid algorithm was observed to be less time-consuming compared to the Fluent Meshing algorithm, as it does not require additional files and parameter setup like the Fluent Meshing and the simulation time was observed to be shorter. However, in the glaze ice case, the discrepancies between the two algorithms are shown. The OptiGrid ice shape displays a slight underestimation of the ice thickness though both remeshing algorithms tend to deliver similar ice shape features. One may conclude that OptiGrid is equally reliable in predicting glaze ice shapes. However, it was observed that when using a finer mesh, the OptiGrid algorithm struggles with very small cell sizes, which led to a failed meshing error report in the 8th shot of the simulation run. Due to OptiGrid's method of node displacement, the more steps are done in the multishot simulation the chances of acquiring either very large or very small cells increase. In the user manual [65], ANSYS recommends using Fluent Meshing for complex geometries. Since the ice shapes of the rotor icing simulations are expected to have an irregular form, Fluent Meshing is decided as the automatic remeshing algorithm for this thesis.

Finally, the effect of the chosen CFD simulation software is observed. There are several CFD icing simulation tools available [62]. However, most CFD tools were developed for application in larger manned aviation. Applicating these tools for smaller, newer aircraft configurations may push the boundaries of their validation range. LEWICE [63] and ANSYS FENSAP-ICE [64] are two CFD icing tools commonly used for studying icing on smaller aerial vehicles. In the scope of this thesis, the simulation model is run using both CFD solvers can be seen in Figure 4.5 that both codes can predict consistent rime ice shapes. However, a stark deviation is observed in the glaze ice shapes. The LEWICE code underpredicts the total ice mass and delivers fewer horn ice features compared to FENSAP-ICE. This is agreeing with the observation by Hann [66] for simulations with the NREL S826 airfoil. The level of

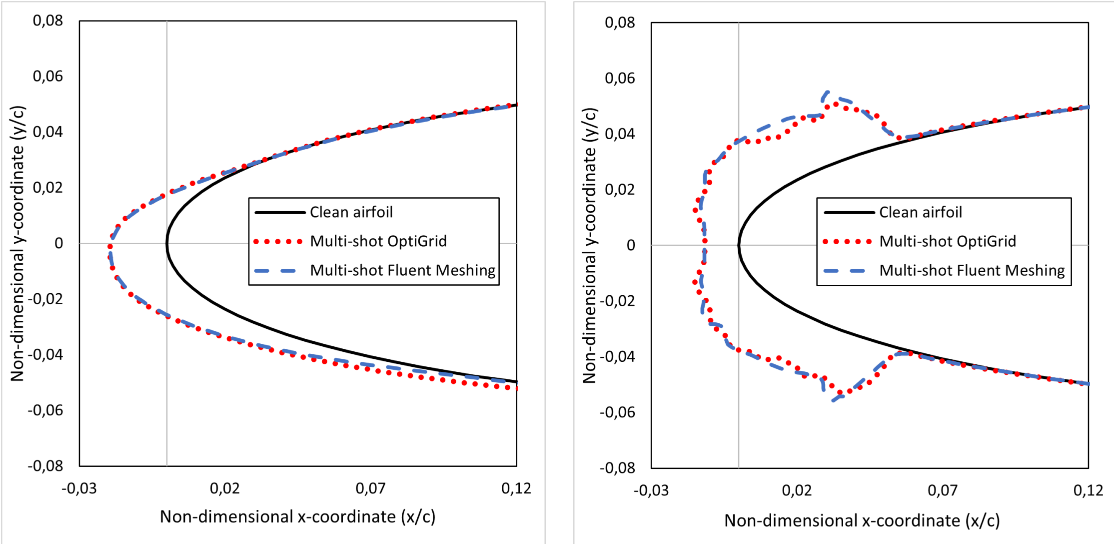

(a) (b)

Figure 4.4: A comparison of the results from multi-shot simulations using OptiGrid and Fluent Meshing automatic remeshing algorithms for the rime (a) and glaze (b) ice case.

aerodynamic penalties due to icing and the heat flux required to mitigate it depends highly on the formed ice shapes as it dictates how the flow physics change [19]. Therefore, capturing the ice features is regarded as important and the use of FENSAP-ICE for the icing simulations is decided.

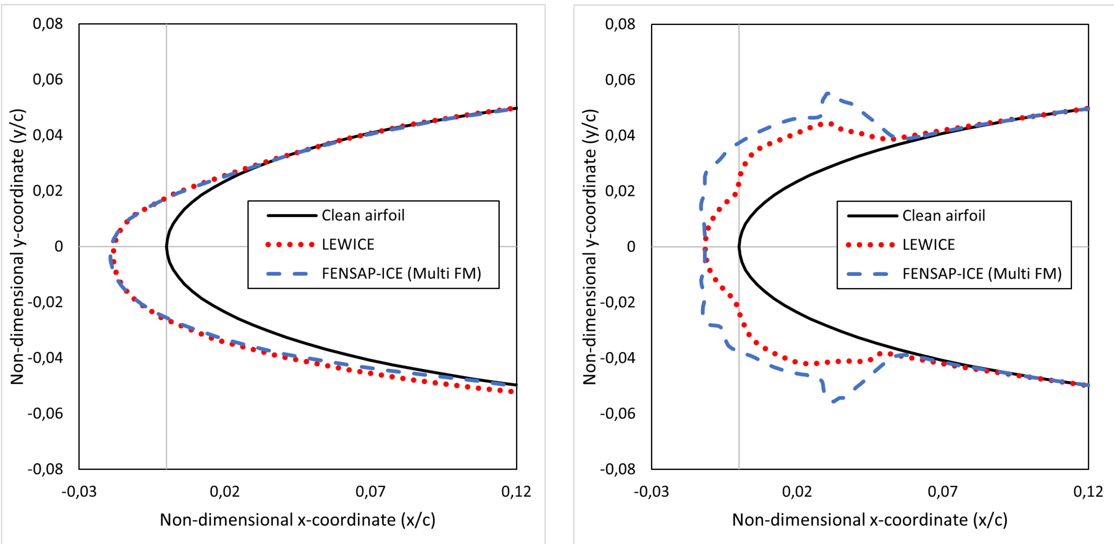

(a) (b)

Figure 4.5: A comparison of the simulation results using LEWICE and FENSAP-ICE codes for the rime (a) and glaze (b) ice case.

4.1.3 Ice Accretion Validation

Following the parameter study, the simulation results are compared to the experimental ice shapes obtained by Han et al. [95]. The numerical ice shapes were obtained using the parameter setup listed in Table 4.2. The icing conditions were set to match the conditions used in the experiments and it is presented in Table 3.2 for both rime and glaze ice cases. The simulations were conducted using the Spalart-Allmaras turbulence model and the flow is set to fully turbulent to take the surface roughness due to ice into account. Despite the recommendation of using Langmuir D droplet distribution for water droplets smaller than 50 μm, a monodisperse distribution was chosen instead since the simulation results using a monodisperse distribution in the work of Fajt et al. [35] is shown to be sufficient.

Table 4.2: Parameter setup for the ice accretion simulation.

FENSAP	
Turbulence model	Spalart-Allmaras
Boundary layer	Fully turbulent
Surface roughness	Specified sand grain 0.0005 m
Artificial viscosity	Streamline upwind + cross wind dissipation 1E−07
DROP3D	
Physical model	Droplets
Distribution	Monodisperse
Water density	1000 kg/m^2
ICE3D	
Ice - Water model	Glaze Advanced
Roughness output	Sand grain from beading
Time step	Automatic
Grid displacement	10 shot multishot, custom Fluent Meshing

The simulation results compared to the experimental data set are presented in Figure 3.3. For the rime ice case, the simulation correctly captures the upper and lower icing limits and the streamlined shape while slightly overestimating the total ice thickness. This difference could be caused by the applied turbulence model which could only approximate the turbulence occurring and not resolve it. However, the simulation can reproduce the general rime ice shape of the experiment with minor discrepancies. Therefore, one may conclude that the simulation model is suitable for rime icing conditions. In the glaze ice case, the ice thickness at the leading edge is shown to be underpredicted by the simulation. The ice shapes at the upper and lower side of the airfoil at approximately 4% of the chord are also significantly less when compared to the experimental results. The pressure side of the airfoil presents more feathering ice shapes in the experiment, which is lacking in the numerical result. This could be caused by the ice

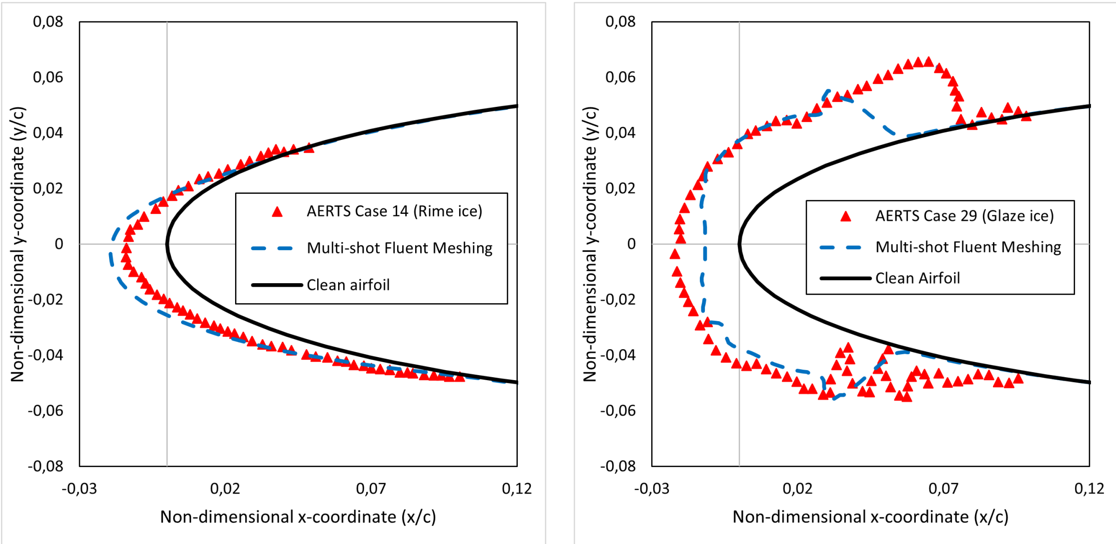

(a) (b)

Figure 4.6: Figure: Results of the NACA 0012 ice accretion simulation in rime (a) and glaze (b) icing conditions in comparison with the AERTS experimental results [95].

horns formed in the numerical ice shapes. The flow field behind an ice horn is characterized by large separation regions [19], thus hindering the ice growth behind the region. Glaze ice shapes are typically more complicated to simulate properly due to the heat transfer, whereas rime ice cases freeze immediately upon collision [40].

Lastly, a repeatability test was conducted to measure the consistency of the simulation results. The glaze ice case was chosen for this test as it is more probable for the ice shapes to grow irregularly in this icing condition and the flow would have more turbulence intensities. The results of both simulation runs are presented in Figure 4.7. The simulation setup for the two runs is the same except for the CFL number and the maximum time step. The first run was set with a CFL number of 50 and a maximum time step of 300, while the second run was set finer with a CFL number of 100 and 1500 maximum time steps. This was done to improve the residual value of the initial run. The results show a good general agreement between the two ice shapes and icing limits. Some discrepancies were found in the formation of the ice horns on both sides of the airfoil with the first simulation predicting a slightly more inclined ice horn. The second simulation also seems to predict a marginally lower thickness at the front of the ice shape. The total ice masses are compared and a difference of 0.376% was found between the two simulations.

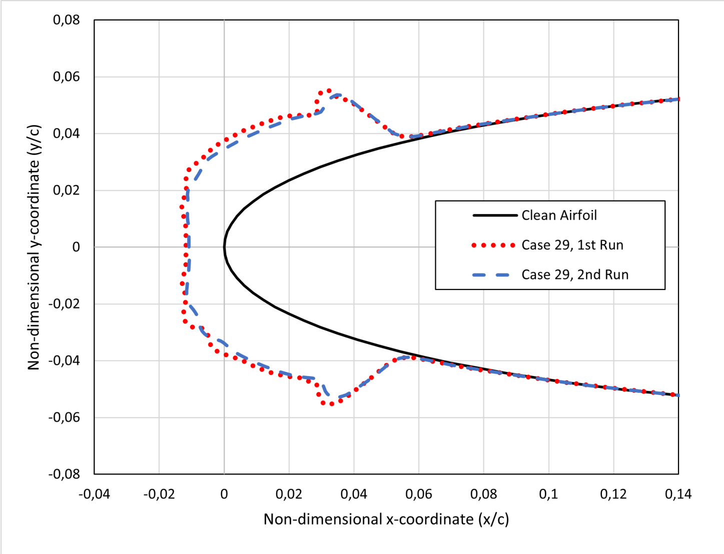

Figure 4.7: Comparison of two NACA 0012 ice accretion simulations with similar simulation and icing conditions, except for the CFL and maximum time step setup.

4.2 Ice Accretion Simulation Results

In the scope of this thesis, 20 ice accretion simulations were conducted for two different eVTOL rotor sizes. The ice accretion study begins with investigating the ice accretion obtained through 2D simulations. The rotor sections in three different radial positions were taken using Siemens NX and exported to Pointwise for mesh generation. The airfoils were calculated in three different types of icing conditions. The icing conditions for the small 15-inch rotor are described in Table 3.8 and for the large 80-inch rotor in Table 3.9. Afterward, a 3D ice accretion simulation is done for each rotor.

4.2.1 2D Simulations

The results of the 2D ice accretion simulations on the 15-inch and 80-inch rotor sections are presented in this subsection. As pictured in Figure 4.10, it can be seen for the 15-inch rotor that all rotor sections show significant ice accumulation in the leading edge of the airfoil. There are no visible ice shapes formed on the suction side of the airfoil, although surface roughness due to ice may occur. Ice accretion has formed along the pressure side of the airfoils on all sections and all tested temperatures. On the outer side of the blade, at 75% and 95% of the blade radius, the ice is shown to build up thicker close to the trailing edge, while the thickness remained constant for the 50% radial position. On the trailing edge itself, there is no ice build-up. Ice horn shapes can be observed in all glaze icing conditions with the most prominent being towards the tip of the blade at 95% radial position. It is observed that the predicted ice shapes for icing temperatures of -10 and -15 °C are similar. In the two colder icing conditions, the simulation predicts a typical rime ice shape for the airfoils closer to the rotor center. At the tip of the blade, the ice accretion formed a small horn on the upper side of the ice. At 95% of the blade radius, the airfoil is considerably smaller and thinner compared to the inner parts of the blade. This leads to a higher droplet collection efficiency. The blade tip also experiences the largest local tangential speed due to rotation, which generally increases the stagnation temperature. However, in the 15-inch case with a simulated rotor rotation of 5000 RPM and an air temperature of -15 °C, the adiabatic stagnation temperature at 95% of the blade radius is -9.921 °C and therefore allowing the water droplets to freeze. It should be mentioned that the icing time of the 95% airfoil in -5 °C was reduced from 120 s to 60 s due to remeshing failures at the 8th multishot step.

Compared to the VTT ice shapes in Figure 3.4, the numerical ice shapes of the 15-inch rotor predict a more rounded shape even for the glaze icing condition, which is typically irregular. The VTT experiments show no ice accretion in the blade tip at -5 °C, contrary to the simulation results. At -10 °C and -15 °C the experiments display the amount of ice accretion similar to the numerical solution, albeit with a varied general shape. The experimental ice shapes in Run 177 display sharp ice horns and feathering despite being tested at a typically rime icing condition. This contrasts the rounded ice shape from the simulations, save from the ice accretion at 95% which approximated the ice accumulation at the leading edge. Looking at the experimental and numerical ice shapes at 75% radius for -5 °C, one may conclude that the simulation is capable of capturing the approximate ice shape and mass though with fewer details captured. Müller et al. [37] investigated the numerical ice accretion on a UAV propeller. At 21 inches, the studied propeller has a slightly larger diameter compared to the 15 inches used in this thesis and in the VTT experiments. Comparing the numerical ice shapes obtained in this study with the shapes from Ref [97], it can be seen that the propeller simulations display more ice horn shapes specifically at -5 °C. At -15 °C, both numerical ice shapes predict a significant amount of ice accretion and in a shape that commonly represents rime ice.

The ice accretion simulation results for the large 80-inch rotor sections are presented in Figure 4.11. In general, the ice shapes obtained differ from the 15-inch rotor sections. The ice accretion at the blade tip in rime icing conditions shows the most similarities between the rotors, as both simulations predict a significant ice accumulation at the leading edge. The ice accretion at the pressure side of the airfoil leading to the trailing edge also shows a similar trend with the 80-inch rotor displaying more ice feathering and a small ice horn at approximately 90% of the chord length. There is no ice accretion at the 95% airfoil for the lower temperatures. This is owed to the adiabatic stagnation temperature, which is influenced by the local Mach number, increasing the local temperature above the freezing point [23]. At -2 °C icing condition, the lack of ice due to the heightened stagnation temperature was similarly observed at the 75% airfoil. At -5 °C, the ice shapes at the inner airfoils form a prominent ice horn at the leading edge and a small spike near the trailing edge. At the same time, the ice accumulated on the pressure side of the airfoil with a constant thick layer at 75%

radius and an irregular shape forming at 50% of the blade. In the rime ice case, the inner airfoils form rather uniform ice shapes without ice horns. For the −2 °C icing condition, the simulation predicts notably less ice accretion compared to other temperatures. However, at 50% blade radius small ice horns were simulated around the upper part of the leading edge, which lead to large flow disturbance aft of the ice as displayed in Figure 4.9. Figure 4.8 offers a zoomed-in illustration of the ice shapes at 50% and 75% blade radius around the leading edge.

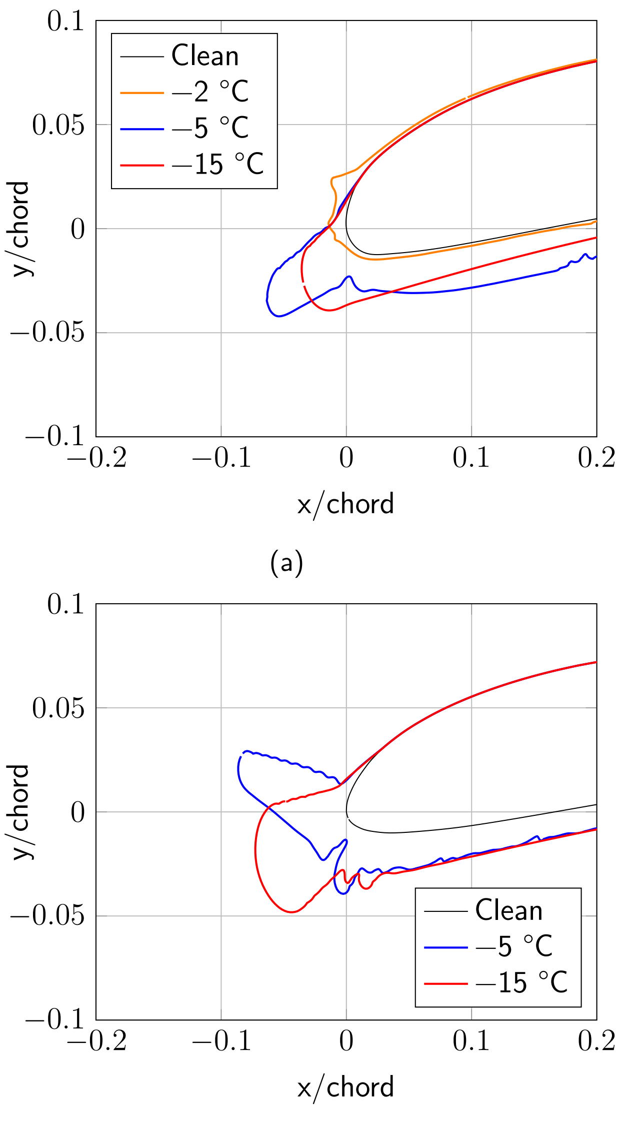

Figure 4.8: Ice accretion on the leading edge of the 80-inch rotor at 50% (a) and 75% (b) of the blade radius.

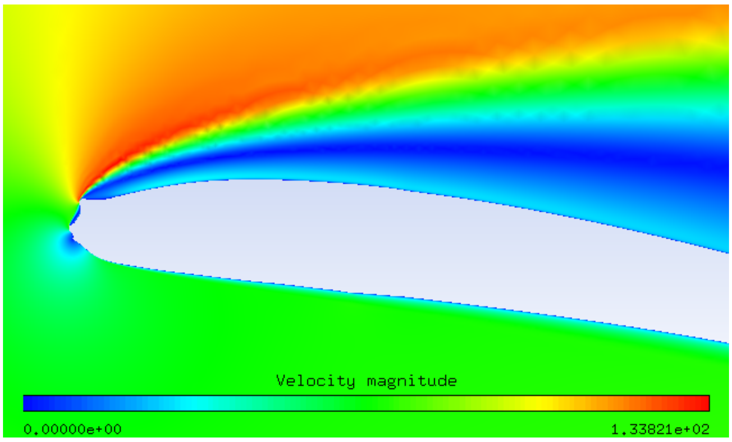

Figure 4.9: Large flow separation following the accreting ice at the leading edge of the 80-inch rotor section at 50% of the blade, glaze icing condition at −2 °C.

4.2.2 3D Simulations

An additional two ice accretion simulations were conducted in 3D for each rotor. The small 15-inch rotor simulation was calculated at −10 °C and with a rotation rate of 5000 RPM for 60 seconds. The large 80-inch rotor simulation was run at −15 °C with 1500 RPM for 300 seconds. 2D cross-sectional cuts were made at the 50%, 75% and 95% blade radius of the 3D ice shape solutions. The ice shapes of the 15-inch rotor are illustrated in Figure 4.12. At −10 °C the ice accretion presents a shape typical of rime ice for all rotor sections. The form appears more rounded compared to the 2D simulation results, which tend to grow longer. The ice from the 3D simulation accumulates more on the upper side of the airfoil leading edge, again contrasting the trend of the 2D simulations. Less ice build-up is observed surrounding the trailing edge of the 3D simulations with the most accretion happening at 95% blade radius. The ice accretion at −10 °C for the 15-inch rotor is seen covering the whole blade length in Figure 4.14a. The two-dimensional ice-shape cuttings of the 80-inch rotor are presented in Figure 4.13. The most significant difference between the 2D and 3D ice accretion simulations is the absence of ice in the outer area of the blade from approximately 80% of the blade radius, as seen in Figure 4.14b. Consequently, there is no ice at 95% blade despite the 2D simulation predicting ice accretion. The airflow solution of the 80-inch rotor simulation in 3D shows positive total temperatures starting from approximately 78% of the blade radius towards the blade tip, as illustrated in Figure 4.15. This coincides with the freezing fraction of the 80-inch rotor and with the calculated ice accretion. The spikes forming at the tip of the large rotor may be an error caused by the boundary setting of the mesh since an ice accretion of this kind has not been observed in real life to the author's knowledge. The ice forming in the inner side of the 80-inch rotor blade appears to have typical rime ice shapes. There is no ice accretion

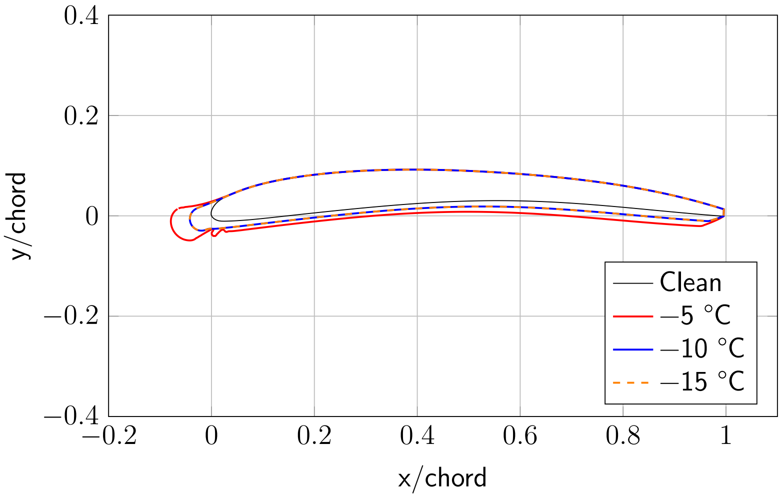

(a) 50% of the blade radius

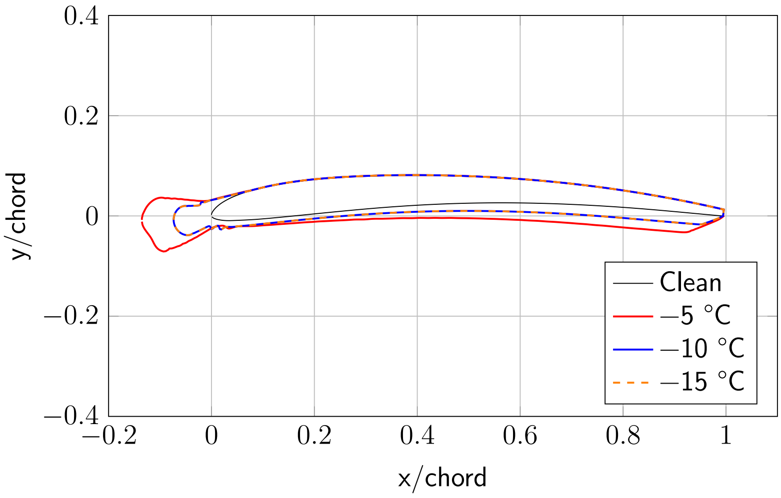

(b) 75% of the blade radius

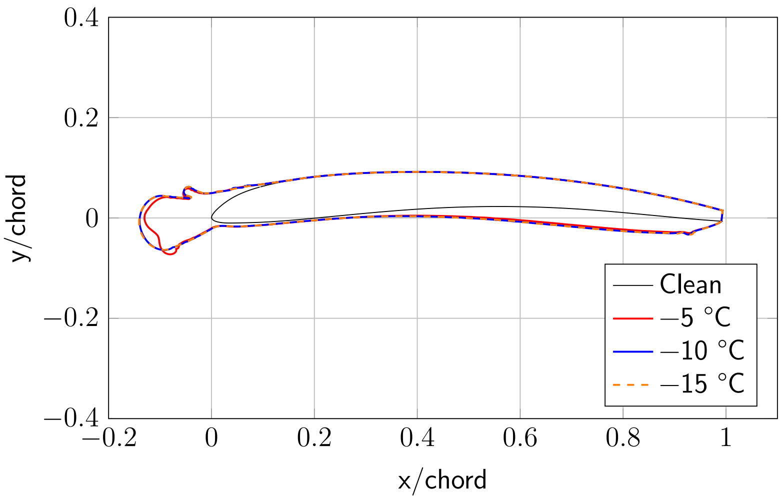

(c) 95% of the blade radius

Figure 4.10: 2D ice accretion simulation results on the 15-inch rotor blade sections.

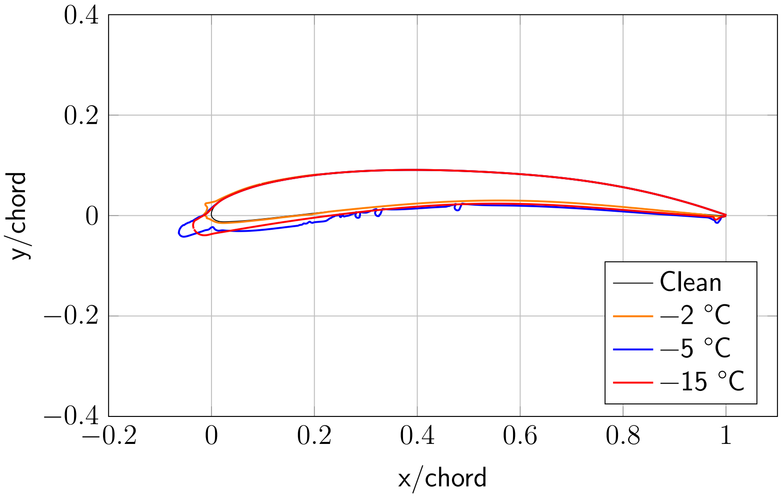

(a) 50% of the blade radius

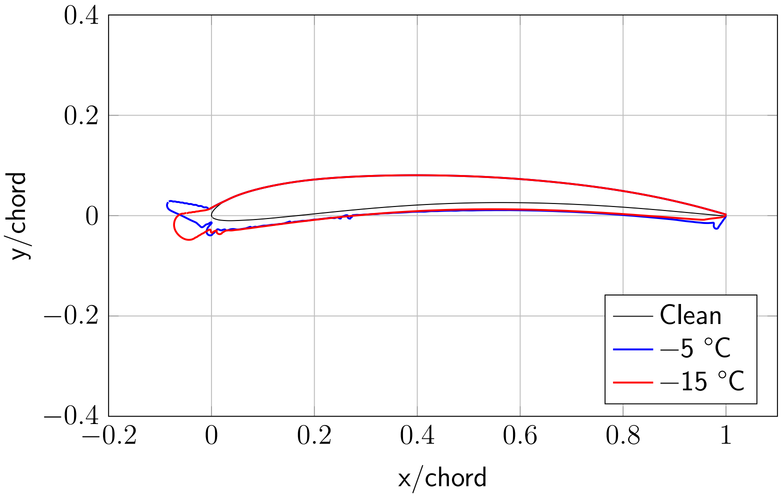

(b) 75% of the blade radius

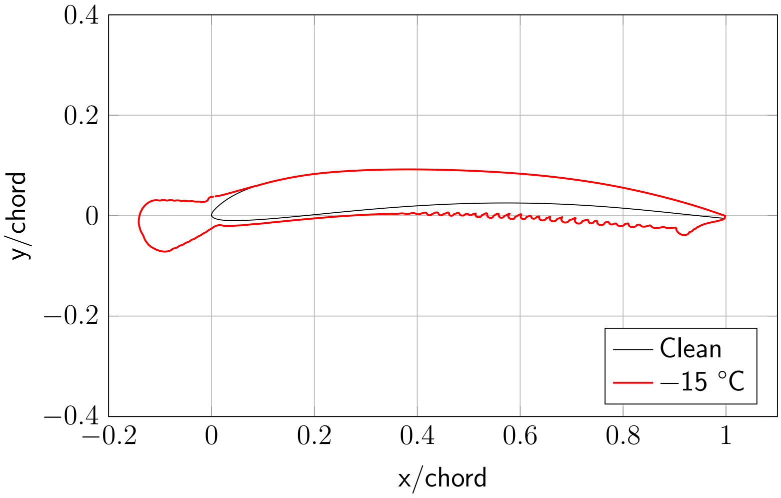

(c) 95% of the blade radius

Figure 4.11: Results of the 2D ice accretion simulation on the 80-inch rotor blade sections.

predicted at the trailing edge of the 75% section, contrasting the 2D solution. The ice on the leading edge appears more streamlined in the 2D results compared to the 3D. At a 50% radius, the ice accumulates more on the upper side of the airfoil leading edge compared to the solutions in 2D.

4.3 Performance Degradation Simulation

Following the ice accretion simulations, the aerodynamic penalties due to icing are investigated in this subsection. This study is done for the -15 °C temperature for both rotors and at the temperature nearest to the freezing point, which would be -5 °C for the 15-inch and -2 °C for the 80-inch rotor. The ice shape and roughness output file obtained from the ice accretion simulation was extracted and the airflow is calculated with FENSAP for the angle of attacks between $-10°$ to $10°$ and considering the local blade twist angle. The performance of the ice-free airfoil is similarly calculated, and the results are compared with the iced airfoil polars. The performance simulations predict an increased drag and reduced lift in the entire range of angle of attack and for all calculated airfoil sections. This is most likely caused by the increased roughness and surface area due to ice accretion and flow separation aft of the ice shape.

Figure 4.16 presents the performance degradation of the small 15-inch rotor section at 75% blade radius. For the rime ice case, a stall angle reduction of approximately 2.5° is observed, as well as a slight performance deterioration along the linear part of the polar. The drag coefficients of the rime ice case experienced the same penalties as the iced airfoil displaying a visible increase compared to the clean airfoil. The glaze ice case displays a more prominent degradation. The stall angle is reduced by roughly 5°, as illustrated in Figure 4.16c. The lift performance along the linear part is reduced even further compared to the rime ice case. Similar behavior is observed for the drag coefficients.

Figure 4.17 displays the aerodynamic penalties of the 80-inch rotor at 75% blade radius for the rime ice case and at 50% for the glaze icing condition. The different rotor sections had to be chosen for the glaze ice case because there was no ice accretion for this icing condition at 75% blade radius. The drag increase for the 80-inch rime ice case appears lesser in comparison to the 15-inch rime, although it is still not negligible as illustrated in Figure 4.17b. The lift reduction caused by rime ice is observed to be greater than the 15-inch rotor section. However, the stall angle reduction is less eminent with a 1° change. The same could not be said for the glaze ice case. Figure 4.17c shows a significant reduction in the lift and the stall angle of the glaze ice case at 50% of the blade. The drag coefficients of the 80-inch 50% airfoil show a noteworthy increase compared to the rime ice case. This could be addressed to the flow separation following the ice horn at the upper side of the leading edge, as presented in Figure 4.9.

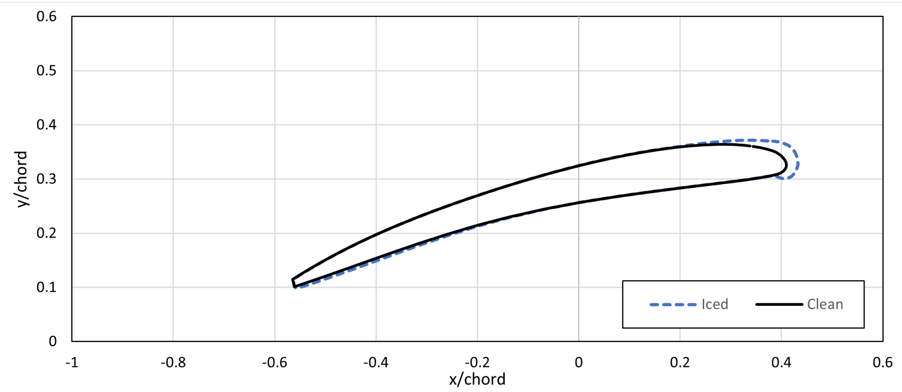

(a) 50% of the blade radius

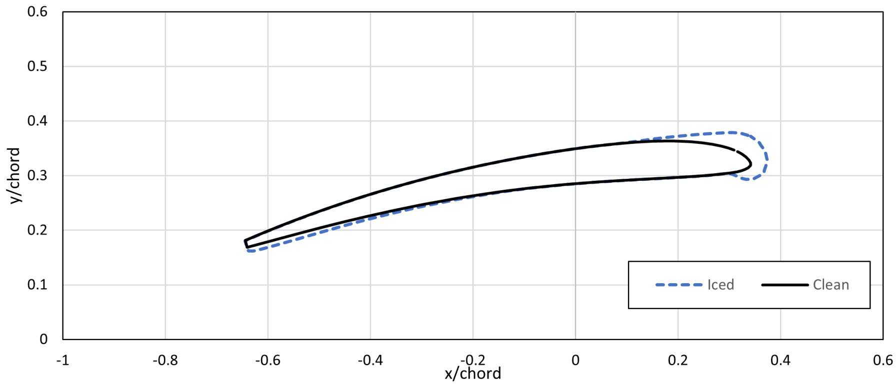

(b) 75% of the blade radius

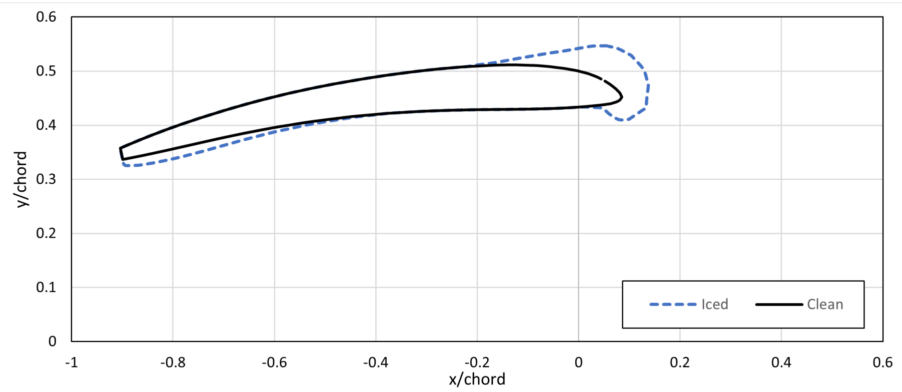

(c) 95% of the blade radius

Figure 4.12: Ice shape cross-sections of the 15-inch rotor obtained from the 3D ice accretion simulation at −10 °C, 5000 RPM, an icing duration of 60 s, an LWC of 0.41 g/m^3, and an MVD of 24.3 μm

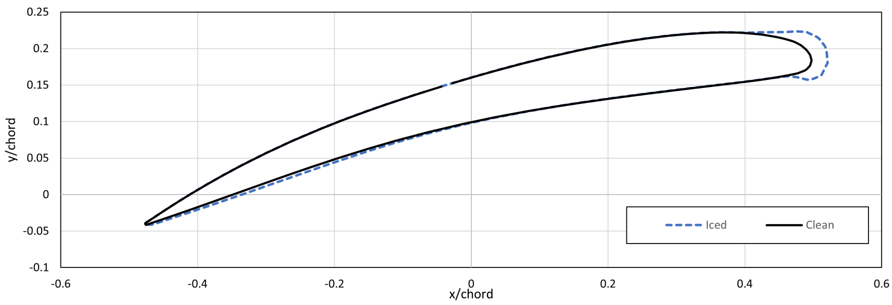

(a) 50% of the blade radius

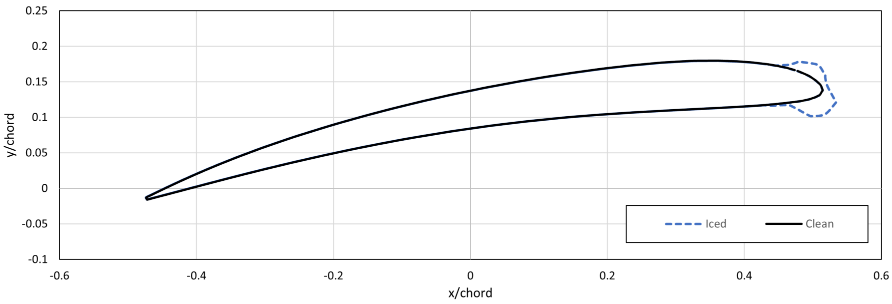

(b) 75% of the blade radius

Figure 4.13: Ice shape cross-sections of the 80-inch rotor obtained from the 3D ice accretion simulation at -15 °C, 1500 RPM, an icing duration of 300 s an LWC of 0.32 g/m^3, and an MVD of 20 μm

(a)

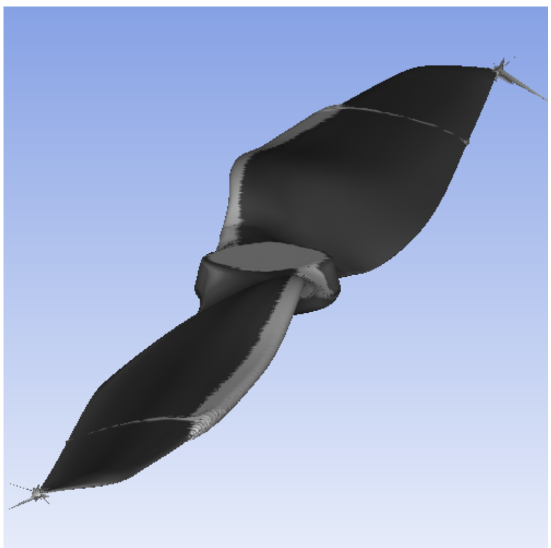

(b)

Figure 4.14: Three dimensional ice shape of the 15-inch rotor at -10 °C (a) and of the 80-inch rotor at -15 °C (b) obtained from a 3D ice accretion simulation.

4.4 Anti-icing Loads Simulation

Considering how the aerodynamic penalties caused by icing influence an eVTOL aircraft, an ice protection system (IPS) is necessary to mitigate the effects of ice accretion. To design and develop a thermal ice protection system, information regarding the required heat flux is required. This can be calculated in the ICE3D module. In general, the ice protection system should produce enough heat to bring the water film to at least 0 °C so no ice can form. Consequently, lower icing conditions would require higher anti-icing loads. For this reason, the IPS requirement simulations were conducted at -15 °C as it is the icing condition that would require the most heat flux for the IPS. There are two heat flux distributions available in FENSAP-ICE: fully evaporate and running wet. The fully evaporative scenario requires enough heat flux to evaporate all impinging water droplets, while the running wet condition sets the surface temperature to 0 °C so water can flow back. This leads to a higher maximum heat flux required for the fully evaporative scenario, as observed in Figure 4.18 for the 15-inch rotor sections and in Figure 4.19 for the 80-inch, where the scenario requires at least double the amount of heat compared to the running wet condition for all blade sections in both rotors. The area where the maximum amount of heat flux is required is located slightly below the tip of the airfoil leading edge. This is where most ice accumulated for this specific icing condition and considering the local blade twist angle. The required heat flux of every rotor section for both conditions is presented in Table 4.3. It is shown that the full evaporative scenario requires around 13% to 43% more heat compared to the running wet condition. For both the 15-inch and 80-inch rotors, the blade tip area requires less heating than the inner sections. This may be attributed to the smaller surface area of the blade's outer section compared to its mid and inner sections.

Table 4.3: Fully evaporative and running wet heat flux requirements for the blade sections of both rotors at an air temperature of -15 °C.

Rotor	Radial position	FE Requirement (W)	RW Requirement (W)	Difference in %
15-inch	50%	5.83	3.47	40
15-inch	75%	4.11	3.02	26
15-inch	95%	1.90	1.65	13
80-inch	50%	122	84.7	30
80-inch	75%	99	60.5	39
80-inch	95%	44.6	25.4	43

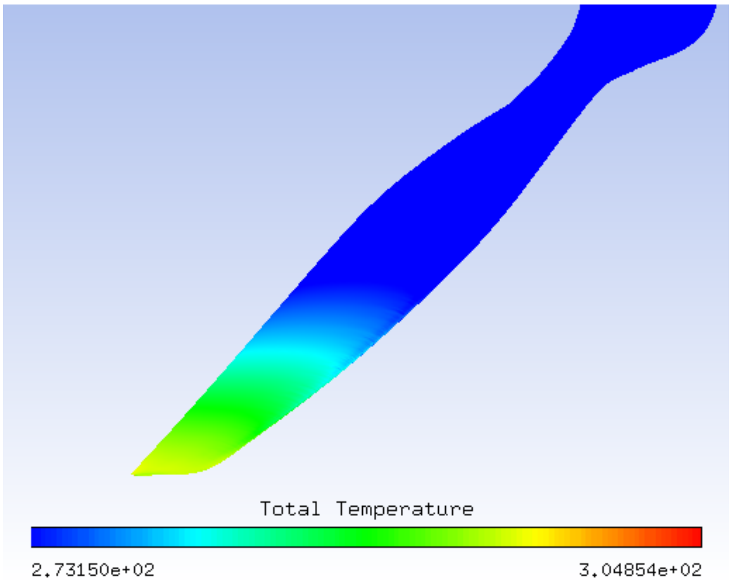

Figure 4.15: Total temperature of the airflow on the 80-inch rotor with deep blue indicating negative temperatures.

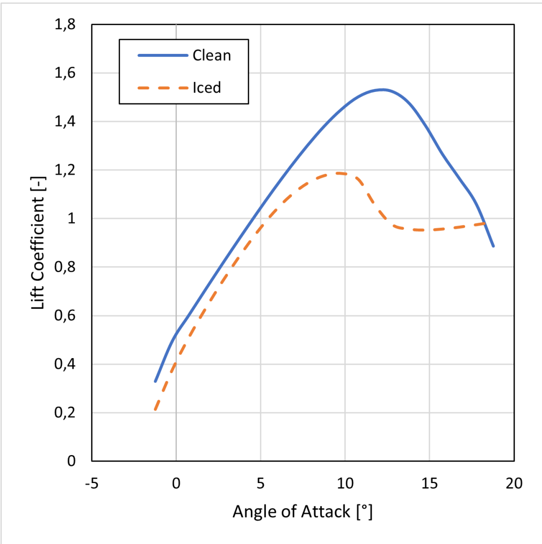

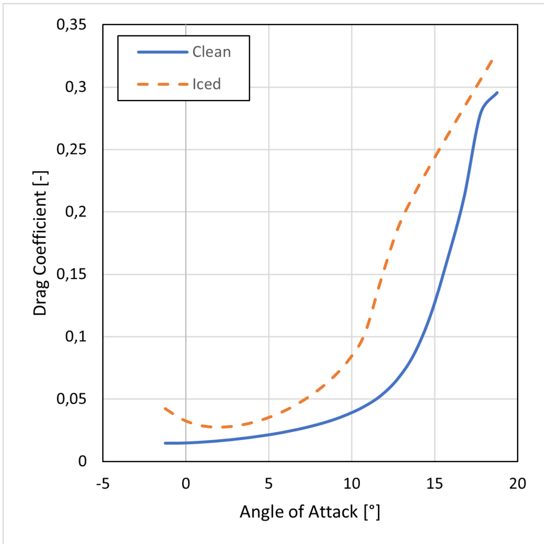

(a) (b)

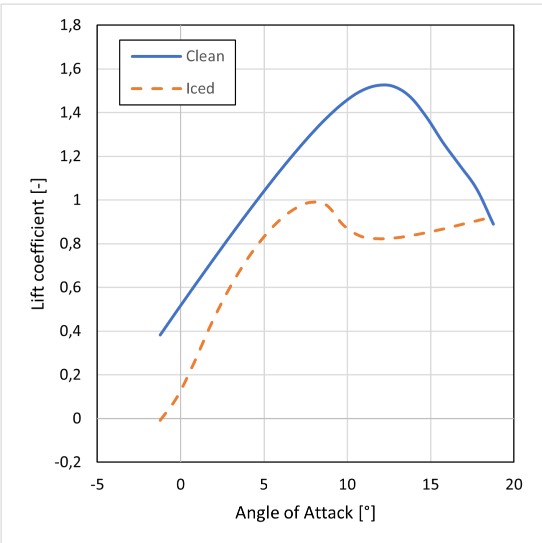

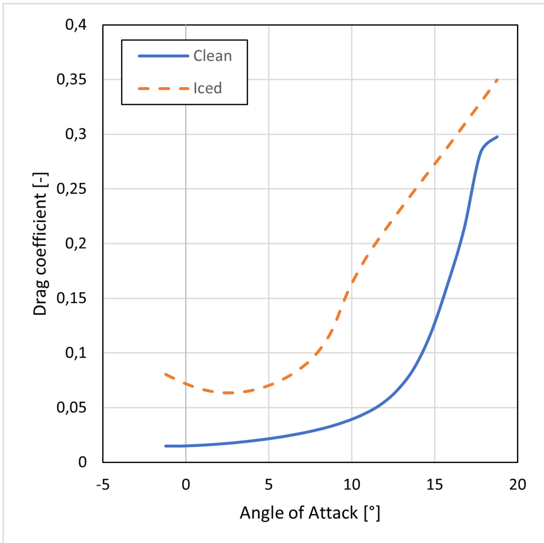

(c) (d)

Figure 4.16: Degradation of the lift coefficient (a, c) and the drag coefficient (b, d) due to ice accretion at −15 °C (a, b) and −5 °C (c, d) of the 15-inch rotor at 75% blade radial distance.

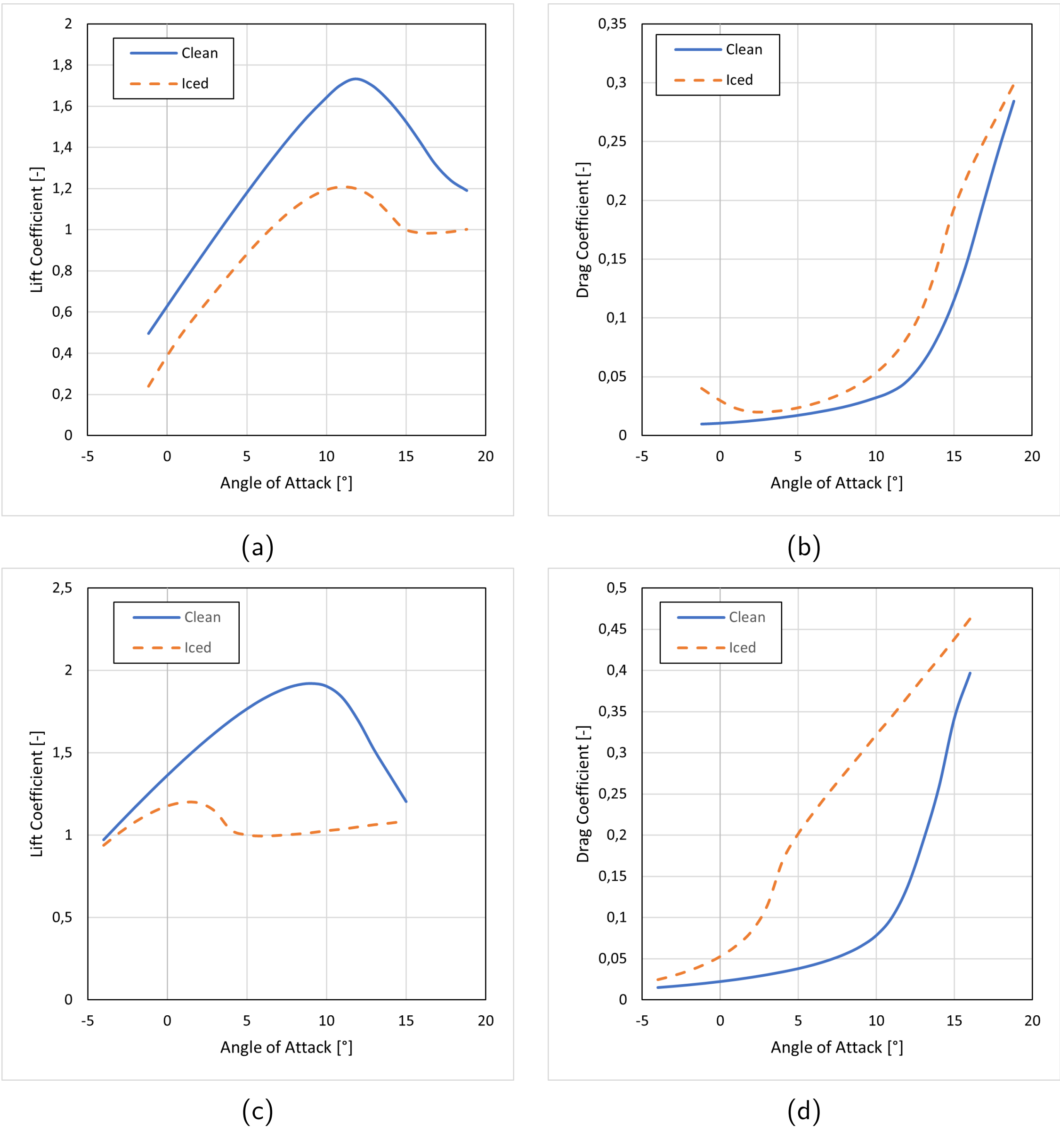

Figure 4.17: Degradation of the lift coefficient (a, c) and the drag coefficient (b, d) of the 80-inch rotor sections due to ice accretion in −15 °C (a, b) at 75% blade radius and −2 °C (c, d) at 50% blade radial distance.

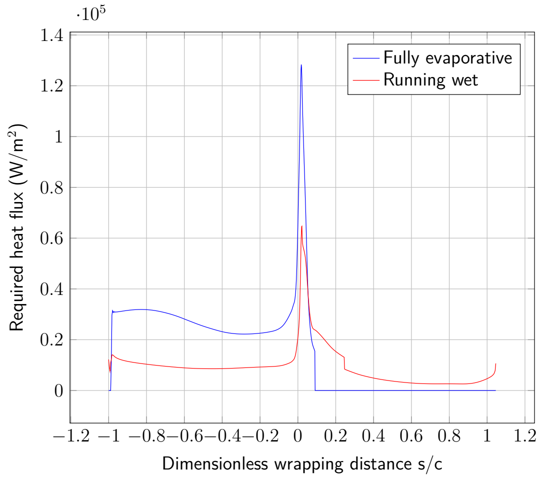

(a) 50% of the blade position

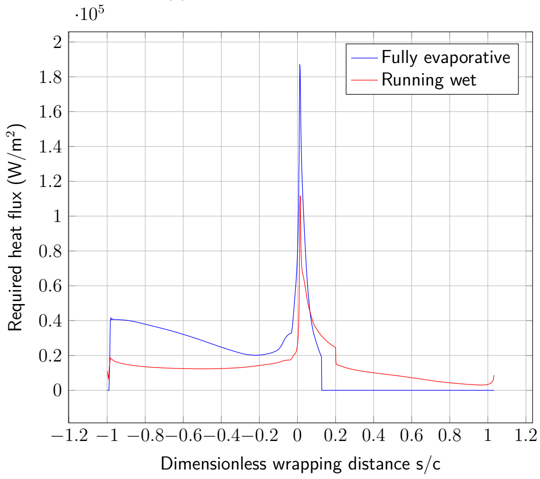

(b) 75% of the blade position

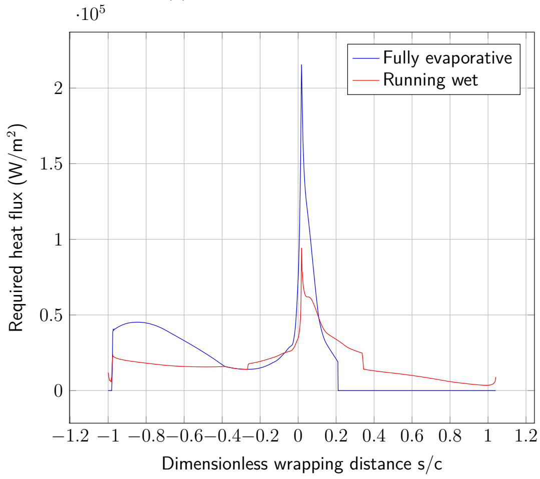

(c) 95% of the blade position

Figure 4.18: Anti-icing load requirements for the 15-inch rotor sections in fully evaporative and running wet conditions at −15 °C.

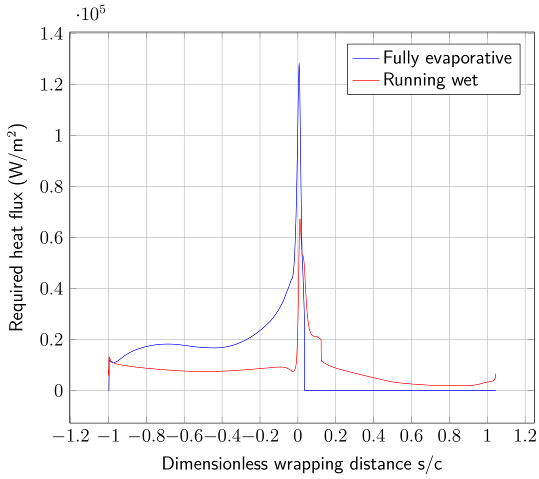

(a) 50% of the blade position

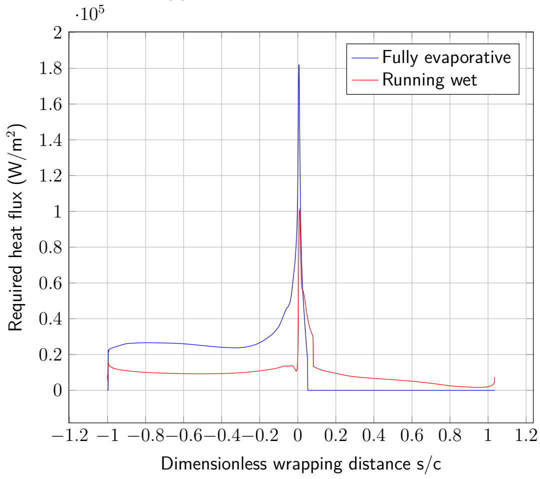

(b) 75% of the blade position

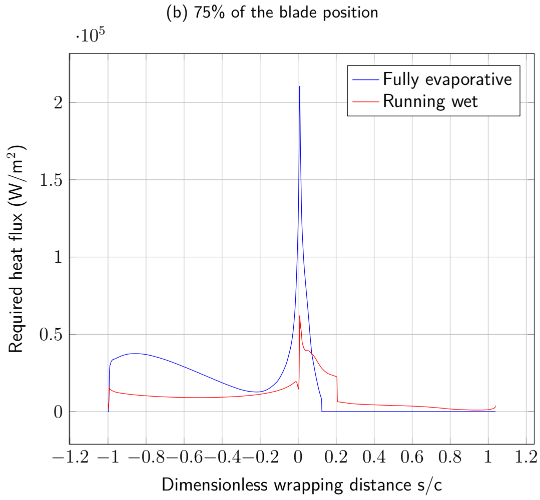

(c) 95% of the blade position

Figure 4.19: Anti-icing load requirements for the 80-inch rotor sections in fully evaporative and running wet conditions at −15 °C.

5 Discussion

The simulation results presented in Chapter 4 are discussed in this chapter. First, a discussion regarding the numerically obtained ice shapes is presented and a possible explanation is considered. Next, the aerodynamic penalty of icing is analyzed. The required anti-icing loads for an ice protection system are explained in the penultimate section. Finally, the uncertainties concerning the work done in the scope of this thesis are presented in the last section.

5.1 Ice Accretion Simulation

The ice accretion simulations were performed for a small 15-inch rotor and a large 80-inch rotor. First, 2D simulations were conducted on the rotor blade sections and then a 3D ice accretion simulation on the whole rotor geometry followed. The results, as presented in Chapter 4, show that the obtained ice shapes depend highly on the icing condition. This agrees with the observation done by Fajt et al. [35] on UAV wings, which has shown that the numerical ice shapes depend on the LWC and MVD. The icing condition dependency of the numerical ice shape is seen, for example, by the similar results obtained from the 15-inch 2D simulation at -10 °C and -15 °C where only the air temperature was different while the icing duration, LWC, and MVD setting are the same.

Results in this thesis are also consistent with the works of Hann and Johansen [32] regarding the influence of airfoil chord length on ice accretion. In the 2D simulations for both rotors in rime icing conditions, the outer blade section at 95% presents the most ice accretion relative to the airfoil size. In low icing temperatures, the water droplets tend to freeze rapidly upon impingement, giving it a generally streamlined ice shape. The airfoil chord length and leading edge diameter at the outer part of the blade are significantly smaller compared to the inner airfoil sections, which gives them less impact on the surrounding far field and consequently leads to a higher collision rate. This and the local airspeed acting on the airfoil lead to a higher ice accretion rate at the tip area of the blade. This supports the observations done by Müller et al. [37], which suggests that the rotational speed of a rotor plays a role in the final ice accretion shape and thus should be treated as an independent parameter. This would again emphasize the sensitivity of rotating lifting surfaces on icing compared to a fixed surface. The ice accretion study on the PX-31 Falk by Fajt et al. [35] was set to an icing duration of 20 minutes and for a significantly larger airfoil, whereas the rotor simulations in this thesis were done at a considerably lower duration, ranging from 1 to 5 minutes of icing time. This would indicate a greater need for icing studies on rotating lifting surfaces, such as rotors and propellers.

Compared to the numerical ice shapes of a UAV propeller studied by Müller et al. [37], the eVTOL small rotor ice shapes show less horn ice formation and more bulky accretion around the leading edge for the −5 °C icing temperature. Large ice accretion means an increase in surface area, which in turn increase the airfoil drag and the droplet accumulation rate. For the ice accretion simulation at −15 °C, both numerical results display a similar typical rime ice shape. This would imply that the direction of airflow with regards to the rotating axis influences the ice shapes in glaze icing conditions particularly. This adds another point to the notion of glaze ice simulation being more challenging to conduct compared to rime, as it has been observed in previous studies [40]. The ice shape cross-section of the 2D simulations in low temperatures generally shows a close approximation with the experimental ice shapes obtained from the VTT test campaign [97], with exception of the sharper details and forming ice feathers. This could imply that a 2D simulation is sufficient to predict the approximate ice shape of a rotor in icing conditions in which rime ice shapes are expected. The 15-inch 3D ice accretion simulation for −10 °C show that the ice formed for the whole blade length. This agrees with the VTT experimental ice shape. However, the 3D simulation predicts a more streamlined ice shape compared to the experiments. This could be caused by the mesh resolution, which may not be sufficiently fine and was not further investigated for grid dependency.

The ice shapes formed on the 80-inch rotor blade sections in temperatures close to the freezing point show great deviation within a variety of icing temperatures and airfoil sizes. At −5 °C, the ice accretion is predicted to have the most mass and grow into highly irregular shapes with horns, which would lead to flow disruption aft of the ice and cause separation. The horn ice forming at −2 °C is shown to cause flow separation as illustrated in Figure 4.9 and lead to significant aerodynamic penalties as presented in Figure 4.17. However, the middle and outer airfoil sections show no ice accretion for −2 °C. As the ice shape dictates how the aerodynamic forces act on the iced rotor blade, further studies on how the ice horns grow in a spanwise direction would be of interest. The 3D ice accretion simulation of the 80-inch rotor in rime ice conditions predicted no ice accretion on the outer parts of the blade. This behavior also prevails in rotors and propellers of larger manned aviation vehicles due to higher stagnation temperatures which lead to substantial local temperature increase [23]. This deviation between the 2D and 3D results could also be caused by increased friction and three-dimensional crossflow, which increases the temperature in the 3D simulation compared to the 2D simulation. The airflow simulation of the large rotor shows positive total temperatures at the outer region of the blade. This would imply that the UAM eVTOL rotor behaves more like rotors in larger manned aviation than that of a UAV. The local Reynolds number of the 80-inch cross-sections ranges between $\mathrm{Re} = 0.95 - 1.18\ 10^6$ depending on chord length, local airspeed velocity, and air temperature. This falls in between the upper range of a typical UAV operational Reynolds number, which is $\mathrm{Re} = 10^4 - 10^7$, and the lower threshold of a larger manned aircraft at $\mathrm{Re} = 10^7 - 10^9$ [29]. As a difference in the Reynolds number directly translates to the different physical behavior of the flow [30], thus influencing the ice accretion process, this must be taken into consideration when investigating potential icing on a UAM eVTOL aircraft. Another important note regarding UAM icing is the influence of the transition mechanism. Some UAM aircraft designs implement a vectored thrust configuration which allows some or all of the rotors to change the direction of the produced thrust. For the rotors, this would mean a transition from a rotational axis perpendicular to the flow direction to parallel, and vice versa. As mentioned in the earlier discussion, a change of flow direction may have implications on the ice accretion in glaze icing conditions. Therefore, an exhaustive study on UAM vehicle icing should include an icing investigation during the transition phase.

A phenomenon that is not considered in this thesis is ice shedding, which is a common occurrence in rotating lifting surfaces due to high centrifugal forces. A detailed analysis regarding ice shedding would require information on the adhesion and cohesion forces acting on the airfoil surface and the ice [45]. In a theoretical scenario where the ice horns formed at $-2°$C do not shed off the blade, it could hinder the rotor performance significantly, especially since the large rotor simulations were conducted under the assumption of vertical take-off and hover flight. It would be interesting to see how the large 80-inch rotor behaves in ambient temperatures close to the freezing point within an experimental framework to provide validation of these ice shape results.

5.2 Performance Degradation Simulation

The effect of icing on an eVTOL aircraft airfoil can be analyzed using the ice shape data and the roughness output file obtained from the ice accretion simulations. The airflow surrounding both clean and iced airfoils is calculated using FENSAP for a range of angles of attack. The study was done for a 15-inch and an 80-inch rotor and for two icing conditions to present a rime and a glaze icing condition. Icing in general serves as a hindrance to aerodynamic performance as it lowers the lift, increases the drag and changes the stall angle [15]. The performance simulation results show that the glaze icing condition experiences a larger deterioration compared to the rime ice case. This could be addressed to the ice horns that typically form in glaze ice conditions for temperatures near the freezing point, while the ice accretion in very low temperatures tends to have a more streamlined shape. It can be seen, for example in Figure 4.9, that the ice horn led to a detachment of flow for the whole remaining airfoil chord length. The flow separates once the boundary layer fails to recover the pressure needed to remain attached to the geometry [19]. This supports the observations made by Bragg et al. [19], stating that horn ice shapes have a significant negative influence on performance degradation due to icing. Although horn and irregular ice shapes are key characteristics of a glaze ice type, the occasion when these shapes occur seems to differ depending on airfoil size, icing condition, and airflow direction. In a previous work by Müller and Hann [45], the studied propeller was observed to form ice horns at -10 °C and $-15°$C. Whereas the small 15-inch rotor in this thesis presents no horn ice at -5 °C nor in the lower temperatures. The geometries studied in both cases have a different size and rotational axis direction, though the LWC is similar with only a 0.03 g/m^3 difference. Previous studies show that the LWC values have an influence on the lift, drag, and moment [35]. The large 80-inch rotor displays an elongated ice horn at -5 °C and a small one on the upper side of the leading edge at -2 °C. These observations would suggest that determining the parameters that influence horn ice accretion, is equally vital to investigate performance degradation due to icing. Moreover, the stagnation point can not be predicted accurately, which might influence the ice horn angles and the ice accretion. Furthermore, the simulations in this thesis were conducted under the assumption of a monodisperse droplet distribution, which is not representative of real-life conditions. The droplet trajectory is influenced by its size since smaller droplets tend to follow the streamline while larger droplets have a more straight-lined flight path [42]. This lead to a higher collision rate with larger droplet sizes. Running an icing study with the Langmuir D distribution, as recommended by the FAA, would offer more realistic ice shapes and consequently more reliable performance data. However, the computational time costs would have to be taken into consideration.

5.3 Anti-icing Loads Simulation

Simulations were done to estimate the required anti-icing loads necessary to thermally mitigate the effects of ice. For an air temperature of -15 °C, the results show very high maximum heat flux requirements for both rotors. Anti-icing is the preferred IPS strategy for rotating lifting surfaces, due to their sensitivity toward aerodynamic penalties due to icing and ice shedding. An electrothermal anti-icing system can run fully evaporative, where the geometry surface is heated as such that all impinging water is evaporated, or running wet, where the surface is heated to 0 °C to prevent ice accretion [15]. As displayed in Figures 4.18 and 4.19, the power requirements of a fully evaporative system are almost double those of a running wet system. However, with a running wet system there is a risk of runback icing, which could acquire due to the liquid water refreezing in areas without heating further down the chord [119]. Runback ice may come in form of a spanwise-ridge shape, which could induce higher levels of aerodynamic penalties even compared to horn ice [19]. Ideally, the heating strips of a fully evaporative system are installed only at the impingement zone, whereas the heat pads in a running wet system should be installed on the blade surface area where water film exists [15]. However, this is not always the case as identifying these zones is a difficult task since they might shift depending on the flight condition. To increase power consumption efficiency, it should be looked into whether implementing both systems into one design is feasible. That way, the IPS mode can be activated depending on the oncoming icing condition. Running wet systems are more energy efficient at temperatures close to freezing point, due to the small temperature difference [15]. Whereas fully evaporative systems may be more suitable for lower temperatures as the area which requires heating is smaller [120]. Alternatively, it may be worthwhile to consider implementing the electrothermal ice protection system in combination with other IPS types, for example, a mechanical IPS type. The most common mechanical de-icing system is pneumatic boots, which are frequently used on the wings and propeller of light manned aircraft [15]. The pneumatic de-icing boots are a mature technology, lightweight and energy efficient [119]. However, the system is known to generate additional drag [121] and the efficiency is affected by large droplets, lower flight speeds, and surface roughness [122]. If the risks of pneumatic boots on an eVTOL rotor and the aircraft's tolerance to intercycle icing are well assessed, its use may be an option worth consideration aside from a fully electrothermal IPS. Although such hybrid systems could pose a challenge for smaller eVTOL drones due to their size, they may be feasible for larger eVTOL aircraft and may be worth consideration. Furthermore, to support the long-term goals of autonomous flights through eVTOL aircraft, an extensive study of icing in diverse meteorological conditions on various aircraft geometries is important for the IPS control systems design and development.

5.4 Uncertainties

Several assumptions were made to simplify the simulations run in the scope of this thesis. For example, the angle of attack in the 2D simulations. The angle of attack is an aerodynamic angle, which can change with the blade pitch angle and is challenging to measure [116]. In a helicopter, most of the changes in the angle of attack are caused by a variation in airspeed or through changes in the climb or descent rate along with rotor blade flapping [116]. The position of the blade during rotation influences the airspeed. The advancing blade experiences an additional velocity component due to wind or forward airspeed, while the retracting blade encounters the exact opposite [116]. This led to a change in airflow velocity across the rotor disk and consequently a change in the local angle of attack. This phenomenon is not considered in the 2D simulations. Furthermore, 2D simulations are not capable of capturing the three-dimensional flow effects such as the blade root effect or the dynamic stall. A 3D simulation could deliver more profound data, albeit with higher computational costs and user experience requirements.

Compared to larger manned aviation, there are fewer validation datasets available for aircraft in the lower Reynolds number regime. Müller and Hann [123] provide an extensive overview of available icing validation datasets. Reynolds number describes the laminar and turbulent state of a flow [69] and a good prediction of the flow transition from laminar to turbulent is important to calculate the energy balance during the icing process [124, 125].

In larger manned aviation, it is assumed that the existence of ice roughness can set off a flow transition to fully turbulent [19]. However, at a lower Reynolds number regime, the boundary layer thickness is larger and therefore, the fully-turbulent flow assumption may not be valid [31].

For the ice accretion simulations, a monodisperse droplet distribution was chosen. This means that the water droplets are assumed to have the same size, which is a state that is most likely not available in real-life cases. The FAA recommends using Langmuir D droplet distribution for cases with an MVD less than 50 μm [41], which is readily implemented within FENSAP-ICE. A more realistic ice shape could be achieved using the Langmuir D distribution, although a spike in the required computational time is to be expected.

The simulations in this thesis were only done on the rotors, while the influence of the rest of the aircraft structure is disregarded. This may have an impact on the forming ice shapes as the airflow approaching the rotors are no longer smooth and potentially disturbed by the aircraft structure or other rotors. Furthermore, several UAM eVTOL aircraft designs available utilize a form of vector thrust. This means that some of the UAM eVTOL rotors are capable of shifting their rotation axis, and this was not regarded in the simulations done within this thesis. Finally, ice-shedding events were not taken into consideration in this study. Centrifugal forces play a significant role in rotating lifting surfaces and can lead to ice shedding. Depending on the type of ice accretion [59], the air temperature [45], the icing duration, and the size of the rotor, the ice shedding effects should not be disregarded.

6 Conclusion

Within this thesis, the effects of icing on eVTOL rotors using CFD simulations were investigated. Two rotors of different sizes were chosen for this study. A small 15x5 inch rotor was chosen to represent eVTOL UAV drones, while a large 80x28 inch rotor was decided to illustrate the rotors used in UAM eVTOL aircraft. Three types of icing simulations were conducted: ice accretion, performance degradation, and anti-icing loads simulation. The CFD simulations in this thesis were conducted using FENSAP-ICE from ANSYS. The software package contains several modules working iteratively to calculate different stages of the icing process. The airflow solution is calculated by the FENSAP module, which utilizes a weak Galerkin finite element method to solve the Reynolds averaged Navier-Stokes equations. The turbulence is modeled using the one equation Spalart-Allmaras turbulence model. The droplet distribution and impingement are calculated using the DROP3D module, which implements an Eulerian two-fluid model. Finally, the ice accretion solution is delivered by the ICE3D module based on the Messinger model. The simulations were done in a multishot set up, dividing the total icing time into 10 smaller steps, and the grid is remeshed between every step using Fluent Meshing. The simulation models were verified and validated against an experimental ice shape dataset of a scaled helicopter rotor blade with a NACA 0012 airfoil cross-section. Two cases were chosen to predict the ice shapes in rime and glaze icing conditions. Three meshes with varying refinement levels were generated to study the grid dependency.

A total of 20 ice accretion simulations were performed for the two eVTOL rotors in various icing conditions. The temperatures range from -2 °C to -15 °C, while the LWC values vary between 0.319 – 0.595 g/m^3. The 2D ice accretion simulations were conducted on the blade cross-sections in the 50%, the 75%, and the 95% radial positions, while the 3D simulations were done on the whole rotor. The ice accretion simulation results agree with the observations of previous works regarding the influence of icing conditions, airfoil chord length, and rotational speed on ice accretion. Compared to a previous study on a UAV propeller, the small eVTOL rotor shows a more rime-like ice shape at -5 °C instead of a glaze ice characteristic. At -15 °C the ice shapes of both rotor and propeller display a typical rime ice shape. This could imply an influence of the rotational axis and airflow direction on the final ice shape in glaze ice conditions. The 2D ice shapes of the small eVTOL rotor in lower temperatures show similarities with the experimental ice shapes obtained from a test campaign in an icing wind tunnel, albeit with fewer details captured. This would suggest that a 2D ice accretion simulation is sufficient for the first assessment in cases where rime ice is expected. The rime ice accretion obtained through 3D simulation also displays a typical rime ice shape, albeit more streamlined, and the ice builds up more on the upper side of the airfoil leading edge. The ice shapes of the large 80-inch rotor blade sections display more variety of ice shapes and horns than the smaller 15-inch rotor, which could indicate a higher sensitivity to icing parameter changes. At -15 °C, the predicted ice shape has a typical rime ice shape with the largest accumulation with regards to airfoil size being at the outer section of the blade. At temperatures near the freezing point, the 80-inch rotor sections demonstrate highly irregular ice shapes with horns. The ice accretion at -5 °C presents the most ice mass and a large horn at the leading edge. The ice horns formed at 50% of the blade radius section for -2 °C are shown to cause large flow disruption aft of the ice, but there is no ice predicted for the middle and outer sections. The 3D simulation of the 80-inch rotor at -15 °C display less ice accretion on the inner sections and no ice at all for the outer region of the blade. This may be caused by the higher stagnation temperature at the tip region of the rotor, which can increase the local temperature significantly and prevent ice from accumulating. This behavior has also been observed in larger manned aviation vehicles [23]. This may suggest, that a UAM eVTOL rotor behaves more like the rotor of a larger manned aircraft than that of a UAV.

For the performance degradation simulations, the lift and drag coefficients of the clean and iced airfoils were calculated for a range of angles of attacks and compared. The results show that the iced airfoil with glaze and horn ice shapes go through a larger performance loss compared to the airfoils with a rime ice shape. It is also observed, that the circumstances in which horn ice develops depend not only on the air temperature but also on airfoil size, droplet parameter, and airflow direction. This would indicate that determining the parameters inducing horn ice accretion is required to be able to predict the performance loss due to icing. Finally, the anti-icing loads required for designing an electrothermal ice protection system were calculated. At an air temperature of -15 °C, the small 15-inch rotor requires a maximum of 180 kW/m^2 of power to evaporate the impinging water droplets, while the large 80-inch rotor needs 170 kW/m^2. The power requirements for a running wet condition are lower, but the risks of runback ice are higher. To lower the IPS power consumption, implementing both anti-icing strategies for different conditions may be looked into. It may also be worthwhile to look into other IPS strategies aside from electrothermal, especially for the larger rotor. In general, there is a need to obtain knowledge regarding the severity of ice in various icing conditions on different aircraft geometries to develop an IPS control system with autonomous capabilities.

Several assumptions were made to simplify the simulation setup. The 2D ice accretion simulations were done at only one angle of attack and neglected the three-dimensional effects due to rotation. The chosen validation data is in a slightly higher Reynolds number regime compared to the large rotor and it is a magnitude larger than the small rotor. The fully turbulent flow assumption may not hold for cases in lower Reynolds numbers. The monodisperse droplet distribution applied within this thesis is rarely observed in real-life situations, if at all. Ice-shedding events, which are prominent in rotating lifting surfaces due to centrifugal forces, are not taken into consideration. Finally, the simulations were done only on the rotor and disregarding the rest of the aircraft structure and its configuration. As several UAM aircraft designs have vectored thrust capabilities, the transition phase should be taken into consideration especially when investigating icing for the whole mission profile.

A good understanding of the ice accretion of the rotor in different icing conditions is essential to investigate the aerodynamic effects of icing on an eVTOL aerial vehicle. Considering the variety of ice shapes obtained in temperatures close to the freezing point and the performance degradation caused, it would be beneficial to conduct future studies for this temperature range. Obtaining additional experimental data would also be an interest as it can validate the simulation results. The sensitivity of the rotor towards various meteorological conditions also needs to be further studied, to provide the necessary information required to mitigate the issues caused by ice.

References

[1] *Dreams of flight*, Science Museum Blog, Section: At the Museum, (Dec. 15, 2017) https://blog.sciencemuseum.org.uk/dreams-of-flight/ (visited on 02/22/2023).

[2] *A history of helicopter flight*, (July 13, 2014) https://web.archive.org/web/20140713201846/http:/terpconnect.umd.edu/~leishman/Aero/history.html#Early_Thinking (visited on 02/22/2023).

[3] J. G. Leishman, *Principles of helicopter aerodynamics*, 2nd ed, Cambridge aerospace series 18, OCLC: ocm61463625 (Cambridge University Press, Cambridge ; New York, 2006), 826 pp.

[4] W. R. Young, *The helicopters*, in collab. with T.-L. Books, The Epic of flight (Time-Life Books, Alexandria, Va, 1982), 175 pp.

[5] *Bell helicopter*, Helis.com, https://www.helis.com/timeline/bell.php (visited on 02/22/2023).

[6] NASAPAV, *NASA puffin low noise, electric VTOL personal air vehicle*, (Nov. 11, 2009) https://www.youtube.com/watch?v=rhpPhvWvLgk (visited on 02/22/2023).

[7] M. Moore, "NASA puffin electric tailsitter VTOL concept", in 10th AIAA aviation technology, integration, and operations (ATIO) conference (Sept. 13, 2010).

[8] B. Seegers, B. Guthrie, and R. Fontana, "Puffin redundant electric propulsion powertrain system", in 10th AIAA aviation technology, integration, and operations (ATIO) conference (Sept. 13, 2010).

[9] L. Gipson, *AAM project national campaign overview*, NASA, (Mar. 12, 2020) http://www.nasa.gov/aeroresearch/aam/description.html (visited on 02/22/2023).

[10] *Urban air mobility: targeting autonomous flight operations from the beginning*, Roland Berger, Last Modified: 2021-08-26T14:15+02:00, https://www.rolandberger.com/en/Insights/Publications/Urban-Air-Mobility-Targeting-autonomous-flight-operations-from-the-beginning.html (visited on 02/15/2023).

[11] E. Alvarado, *The vision of advanced air mobility (AAM)*, Section: Reports, (Feb. 3, 2023) https://droneii.com/advanced-air-mobility-aam-evtol-vertiports-utm (visited on 02/22/2023).

[12] *eVTOL timeline*, https://evtol.news/resources/evtol-timeline (visited on 02/22/2023).

[13]R. Goyal, D. C. Reiche, C. Fernando, J. D. Jacquie Serrao, D. S. Kimmel, A. Cohen, and S. Shaheen, "Urban air mobility (UAM) market study - booz allen hamilton technical briefing", NTRS Author Affiliations: Booz Allen Hamilton (United States), University of California, Berkeley NTRS Report/Patent Number: HQ-E-DAA-TN64105 NTRS Document ID: 20190000517 NTRS Research Center: Headquarters (HQ).

[14]*The high-flying industry: urban air mobility takes off*, Roland Berger, Last Modified: 2021-07-26T15:42+02:00, https://www.rolandberger.com/en/Insights/Publications/The-high-flying-industry-Urban-Air-Mobility-takes-off.html (visited on 11/11/2022).

[15]R. Hann and T. Johansen, *Unsettled topics in unmanned aerial vehicle icing* (SAE International, Apr. 27, 2020).

[16]*Engine icing - glenn research center | NASA*, Glenn Research Center | NASA, https://www1.grc.nasa.gov/aeronautics/icing/engine-icing/ (visited on 02/22/2023).

[17]*Airframe icing - glenn research center | NASA*, https://www1.grc.nasa.gov/aeronautics/icing/airframe-icing/ (visited on 02/22/2023).

[18]*14 CFR appendix c to part 25 - appendix c to part 25*, LII / Legal Information Institute, https://www.law.cornell.edu/cfr/text/14/appendix-C_to_part_25 (visited on 02/22/2023).

[19]M. Bragg, A. Broeren, and L. Blumenthal, "Iced-airfoil aerodynamics", Progress in Aerospace Sciences **41**, 323–362 (2005).

[20]B. C. Bernstein, C. A. Wolff, and F. McDonough, "An inferred climatology of icing conditions aloft, including supercooled large drops. part i: canada and the continental united states", Journal of Applied Meteorology and Climatology **46**, 1857–1878 (2007).

[21]B. C. Bernstein and C. Le Bot, "An inferred climatology of icing conditions aloft, including supercooled large drops. part II: europe, asia, and the globe", Journal of Applied Meteorology and Climatology **48**, 1503–1526 (2009).

[22]K. L. Sørensen, K. T. Borup, R. Hann, B. Bernstein, and M. Hansbø, *UAV atmospheric icing limitations: climate report for norway and surrounding regions* (UBIQ Aerospace, 2021).

[23]R. W. Gent, N. P. Dart, and J. T. Cansdale, "Aircraft icing", Philosophical Transactions of the Royal Society of London. Series A: Mathematical, Physical and Engineering Sciences **358**, edited by G. Poots, 2873–2911 (2000).

[24]F. T. Lynch and A. Khodadoust, "Effects of ice accretions on aircraft aerodynamics", Progress in Aerospace Sciences **37**, 669–767 (2001).

[25]R. Flemming, "The past twenty years of icing research and development at sikorsky aircraft", in 40th AIAA aerospace sciences meeting & exhibit (Jan. 14, 2002).

[26]R. A. Siquig, *Impact of icing on unmanned aerial vehicle (UAV) operations*, Section: Technical Reports ().

[27]D. Haulman, *U.s. unmanned aerial vehicles in combat, 1991-2003*, Section: Technical Reports ().

[28]L. Peck, C. Ryerson, and C. J. Martel, *Army aircraft icing*, Report, Accepted: 2016-03-21T16:37:08Z (Cold Regions Research and Engineering Laboratory (U.S.), Sept. 2002).

[29]R. Hann and J. Wallisch, *UAV database*, in collab. with R. Hann and N. U. O. S. bibinitperiod Technology, Type: dataset, 2020.

[30]K. Szilder and S. McIlwain, "In-flight icing of UAVs - the influence of reynolds number on the ice accretion process", in (Oct. 18, 2011), pp. 2011–01–2572.

[31]R. Hann, "UAV icing: challenges for computational fluid dynamic (CFD) tools", in (July 2022).

[32]R. Hann and T. A. Johansen, "UAV icing: the influence of airspeed and chord length on performance degradation", Aircraft Engineering and Aerospace Technology **93**, 832–841 (2021).

[33]Y. Liu, L. Li, W. Chen, W. Tian, and H. Hu, "An experimental study on the aerodynamic performance degradation of a UAS propeller model induced by ice accretion process", Experimental Thermal and Fluid Science **102**, 101–112 (2019).

[34]S. Yan, T. I. Opazo, J. W. Langelaan, and J. L. Palacios, "Experimental evaluation and flight simulation of coaxial-rotor vehicles in icing clouds", Journal of the American Helicopter Society **65**, 1–15 (2020).

[35]N. Fajt, R. Hann, and T. Lutz, "The influence of meteorological conditions on the icing performance penalties on a UAV airfoil", (2019).

[36]N. Williams, A. Benmeddour, G. Brian, and M. Ol, "The effect of icing on small unmanned aircraft low reynolds number airfoils", in 17th australian international aerospace congress : AIAC 2017, ISSN: 9781922107855 (), pp. 19–25.

[37]N. Müller, R. Hann, and T. Lutz, "UAV icing: numerical simulation of propeller ice accretion", in AIAA AVIATION 2021 FORUM (Aug. 2, 2021).

[38]R. Scavuzzo, M. Chu, and V. Ananthaswamy, "Influence of aerodynamic forces in ice shedding", in 29th aerospace sciences meeting (Jan. 7, 1991).

[39]*UBIQ*, Ubiq, `https://www.ubiqaerospace.com` (visited on 02/22/2023).

[40]R. Hann, "Atmospheric ice accretions, aerodynamic icing penalties, and ice protection systems on unmanned aerial vehicles", Doctoral Thesis (Norwegian University of Science and Technology, Trondheim, Norway, July 2020).

[41]*AC 91-74b - pilot guide: flight in icing conditions*.

[42]L. Battisti, *Wind turbines in cold climates: icing impacts and mitigation systems*, Google-Books-ID: GTi2BgAAQBAJ (Springer, Feb. 16, 2015), 355 pp.

[43]Z. A. Janjua, B. Turnbull, S. Hibberd, and K.-S. Choi, "Mixed ice accretion on aircraft wings", Physics of Fluids **30**, 027101 (2018).

[44]R. J. Kind, M. G. Potapczuk, A. Feo, C. Golia, and A. D. Shah, "Experimental and computational simulation of in-flight icing phenomena", Progress in Aerospace Sciences **34**, 257–345 (1998).

[45]N. C. Müller and R. Hann, "UAV icing: a performance model for a UAV propeller in icing conditions", in AIAA AVIATION 2022 forum (June 27, 2022).

[46]I. B. Laskowitz, "Vertical take-off and landing (VTOL) rotorless aircraft with inherent stability", Annals of the New York Academy of Sciences **93**, 3–24 (1961).

[47]W. Ng, M. Patil, and A. Datta, "Hydrogen fuel cell and battery hybrid architecture for range extension of electric VTOL (eVTOL) aircraft", Journal of the American Helicopter Society **66**, 1–13 (2021).

[48]*Advanced air mobility and urban air mobility | federal aviation administration*, https://www.faa.gov/uas/advanced_operations/urban_air_mobility (visited on 11/27/2022).

[49]*Vectored thrust*, Glenn Research Center | NASA, https://www1.grc.nasa.gov/beginners-guide-to-aeronautics/vectored-thrust/ (visited on 02/22/2023).

[50]A. Straubinger, R. Rothfeld, M. Shamiyeh, K.-D. Büchter, J. Kaiser, and K. O. Plötner, "An overview of current research and developments in urban air mobility – setting the scene for UAM introduction", Journal of Air Transport Management **87**, 101852 (2020).

[51]A. Bacchini and E. Cestino, "Electric VTOL configurations comparison", 26 (2019).

[52]*eVTOL aircraft directory*, https://evtol.news/aircraft (visited on 02/21/2023).

[53]*Operation of unmanned aircraft systems in very low level airspace*, https://www.eurocockpit.be/positions-publications/operation-unmanned-aircraft-systems-very-low-level-airspace (visited on 02/22/2023).

[54]*Joby aviation | joby*, https://www.jobyaviation.com/ (visited on 02/21/2023).

[55]*Archer*, https://archer.com/Midnight (visited on 02/21/2023).

[56]*Volocopter*, Volocopter, https://www.volocopter.com/ (visited on 02/21/2023).

[57]B. P. Hill, D. DeCarme, M. Metcalfe, C. Griffin, S. Wiggins, C. Metts, B. Bastedo, M. D. Patterson, and N. L. Mendonca, *UAM vision concept of operations (ConOps) UAM maturity level (UML) 4*, NTRS Author Affiliations: Deloitte (United States), Langley Research Center, National Aeronautics and Space Administration NTRS Document ID: 20205011091 NTRS Research Center: Headquarters (HQ) (Dec. 2, 2020).

[58]M. Cheung, R. Hann, and T. A. Johansen, "UAV icing: a unified icing severity index derived from performance degradation", in AIAA AVIATION 2022 forum (June 27, 2022).

[59]P. Pellicano, C. Dumont, T. Smith, and J. Riley, *Propeller icing tunnel test on a full-scale turboprop engine*, Data Report DOT/FAA/AR-06/60 (FAA, Mar. 2010).

[60]J. Wallisch and R. Hann, "UAV icing: experimental investigation of ice shedding times with an electrothermal de-icing system", in AIAA AVIATION 2022 forum (June 27, 2022).

[61]R. W. Fox, A. T. McDonald, and J. W. Mitchell, *Introduction to fluid mechanics*, Google-Books-ID: v4T3DwAAQBAJ (John Wiley & Sons, June 30, 2020), 608 pp.

[62]E. Laurendeau, S. Bourgault-Cote, I. A. Ozcer, R. Hann, E. Radenac, and A. Pueyo, "Summary from the 1st AIAA ice prediction workshop", in AIAA AVIATION 2022 forum (June 27, 2022).

[63]*LEWICE3d, version 3.63(LEW-19433-1) | NASA software catalog*, `https://software.nasa.gov/software/LEW-19433-1` (visited on 02/21/2023).

[64]*Ansys FENSAP-ICE | in-flight aircraft icing simulation*, `https://www.ansys.com/products/fluids/ansys-fensap-ice` (visited on 02/22/2023).

[65]*ANSYS FENSAP-ICE user manual*, Jan. 2021.

[66]R. Hann, R. J. Hearst, L. R. Sætran, and T. Bracchi, "Experimental and numerical icing penalties of an s826 airfoil at low reynolds numbers", Aerospace **7**, Number: 4 Publisher: Multidisciplinary Digital Publishing Institute, 46 (2020).

[67]H. Beaugendre, F. Morency, and W. G. Habashi, "FENSAP-ICE's three-dimensional in-flight ice accretion module: ICE3d", Journal of Aircraft **40**, Publisher: American Institute of Aeronautics and Astronautics _eprint: https://doi.org/10.2514/2.3113, 239–247 (2003).

[68]R. Schwarze, *CFD-modellierung: grundlagen und anwendungen bei strömungsprozessen* (Springer Berlin Heidelberg Imprint Springer, Berlin, Heidelberg, 2013).

[69]J. D. Anderson, *Fundamentals of aerodynamics*, Sixth edition, McGraw-Hill series in aeronautical and aerospace engineering (McGraw Hill Education, New York, NY, 2017), 1130 pp.

[70]C.-D. Munz and T. Westermann, *Numerische Behandlung gewöhnlicher und partieller Differenzialgleichungen: Ein anwendungsorientiertes Lehrbuch für Ingenieure* (Springer, Berlin, Heidelberg, 2019).

[71]N. Fallah, C. Bailey, M. Cross, and G. Taylor, "Comparison of finite element and finite volume methods application in geometrically nonlinear stress analysis", Applied Mathematical Modelling **24**, 439–455 (2000).

[72]E. W. Weisstein, *Finite element method*, Publisher: Wolfram Research, Inc., `https://mathworld.wolfram.com/` (visited on 02/23/2023).

[73]E. W. Weisstein, *Finite volume method*, Publisher: Wolfram Research, Inc., https://mathworld.wolfram.com/ (visited on 02/23/2023).

[74]K. H. Huebner, D. L. Dewhirst, D. E. Smith, and T. G. Byrom, *The finite element method for engineers*, Google-Books-ID: g6KSEAAAQBAJ (John Wiley & Sons, Sept. 7, 2001), 745 pp.

[75]W. G. Habashi, F. Morency, and H. Beaugendre, "FENSAP-ICE: a second generation 3d CFD-based in-flight icing simulation system", in (June 16, 2003), pp. 2003–01–2157.

[76]F. Morency, H. Beaugendre, G. Baruzzi, and W. Habashi, "FENSAP-ICE - a comprehensive 3d simulation system for in-flight icing", in 15th AIAA computational fluid dynamics conference (June 11, 2001).

[77]I. Eames and J. B. Flor, "New developments in understanding interfacial processes in turbulent flows", Philosophical Transactions of the Royal Society A: Mathematical, Physical and Engineering Sciences **369**, 702–705 (2011).

[78]A. Jameson, "Multigrid algorithms for compressible flow calculations", in Multigrid methods II, edited by W. Hackbusch and U. Trottenberg, Lecture Notes in Mathematics (1986), pp. 166–201.

[79]A. Favre, "Equations des gaz turbulents compressibles", J. de Mecanique **4** (1965).

[80]J. Blazek, *Computational fluid dynamics: principles and applications* (Butterworth-Heinemann, Apr. 23, 2015), 466 pp.

[81]*Turbulence modeling resource*, https://turbmodels.larc.nasa.gov/ (visited on 02/23/2023).

[82]P. Spalart and S. Allmaras, "A one-equation turbulence model for aerodynamic flows", in 30th aerospace sciences meeting and exhibit (Jan. 6, 1992).

[83]D. C. Wilcox, "Formulation of the k-w turbulence model revisited", AIAA Journal **46**, 2823–2838 (2008).

[84]F. R. Menter, "Two-equation eddy-viscosity turbulence models for engineering applications", AIAA Journal **32**, 1598–1605 (1994).

[85]I. Ozcer, D. Switchenko, G. S. Baruzzi, and J. Chen, "Multi-shot icing simulations with automatic re-meshing", in (June 10, 2019), pp. 2019–01–1956.

[86]Y. Bourgault, Z. Boutanios, and W. G. Habashi, "Three-dimensional eulerian approach to droplet impingement simulation using FENSAP-ICE, part 1: model, algorithm, and validation", Journal of Aircraft **37**, Publisher: American Institute of Aeronautics and Astronautics _eprint: https://doi.org/10.2514/2.2566, 95–103 (2000).

[87]Y. Bourgault, W. G. Habashi, J. Dompierre, and G. S. Baruzzi, "A finite element method study of eulerian droplets impingement models", International Journal for Numerical Methods in Fluids **29**, _eprint: https://onlinelibrary.wiley.com/doi/pdf/10.1002/%28SICI%291097-0363%2819990228%2929%3A4%3C429%3A%3AAID-FLD795%3E3.0.CO%3B2-F, 429–449 (1999).

[88]H. Beaugendre, F. Morency, and W. G. Habashi, "Development of a second generation in-flight icing simulation code", Journal of Fluids Engineering **128**, 378–387 (2005).

[89]Y. Bourgault, H. Beaugendre, and W. G. Habashi, "Development of a shallow-water icing model in FENSAP-ICE", Journal of Aircraft **37**, Publisher: American Institute of Aeronautics and Astronautics _eprint: https://doi.org/10.2514/2.2646, 640–646 (2000).

[90]B. Messinger, "Equilibrium temperature of an unheated icing surface as a function of air speed", Journal of the Aeronautical Sciences **20**, Publisher: American Institute of Aeronautics and Astronautics _eprint: https://doi.org/10.2514/8.2520, 29–42 (1953).

[91]F. Morency, F. Tezok, and I. Paraschivoiu, "Anti-icing system simulation using CANICE", Journal of Aircraft **36**, 999–1006 (1999).

[92]*Overview of CFD verification & validation*, `https://www.grc.nasa.gov/www/wind/valid/tutorial/tutorial.html` (visited on 10/14/2022).

[93]*Verification assessment*, `https://www.grc.nasa.gov/www/wind/valid/tutorial/verassess.html` (visited on 02/23/2023).

[94]*Validation assessment*, `https://www.grc.nasa.gov/www/wind/valid/tutorial/valassess.html` (visited on 02/23/2023).

[95]Y. Han, J. L. Palacios, and E. C. Smith, "An experimental correlation between rotor test and wind tunnel ice shapes on NACA 0012 airfoils", in (June 13, 2011), pp. 2011–38–0092.

[96]*Adverse environment rotor test stand (AERTS) | penn state engineering*, `https://www.aero.psu.edu/research/facilities-and-labs/adverse-environment-rotor-test-stand.aspx` (visited on 02/23/2023).

[97]H. Heramarwan, N. Müller, and R. Hann, *UAM icing: ice accretion experiments and simulation of eVTOL rotors (manuscript submitted for publication)*, 2023.

[98]M. Tiihonen, T. Jokela, L. Makkonen, and G.-J. Bluemink, "VTT icing wind tunnel 2.0: winterwind international wind energy conference", Winterwind Presentations 2016 (2016).

[99]*Agisoft metashape: agisoft metashape*, `https://www.agisoft.com/` (visited on 02/23/2023).

[100]*Mejzlik.eu - design and manufacturing top-quality propellers*, `https://www.mejzlik.eu/` (visited on 02/11/2023).

[101]M. Selig, *UIUC airfoil data site* (Urbana, Ill. : Department of Aeronautical and Astronautical Engineering University of Illinois at Urbana-Champaign, 1996-, 1996).

[102] *NX | siemens software*, Siemens Digital Industries Software, `https://www.plm.automation.siemens.com/global/en/products/nx/` (visited on 02/23/2023).

[103] *Fidelity pointwise*, `https://www.cadence.com/en_US/home/tools/system-analysis/computational-fluid-dynamics/pointwise.html` (visited on 02/23/2023).

[104] *Unstructured domains, t-rex tab*, `https://www.pointwise.com/user-manual/grid/solve/unstructured-domains/t-rex.html` (visited on 02/20/2023).

[105] M. Drela, "XFOIL: an analysis and design system for low reynolds number airfoils", in Low reynolds number aerodynamics, edited by T. J. Mueller, Lecture Notes in Engineering (1989), pp. 1–12.

[106] *Propeller data | mejzlik.eu*, `https://www.mejzlik.eu/technical-data/propeller_data` (visited on 02/11/2023).

[107] P. J. Roache, *Verification and validation in computational science and engineering* (Hermosapublishers, Albuquerque, N.M, 1998), 446 pp.

[108] *Examining spatial (grid) convergence*, `https://www.grc.nasa.gov/WWW/wind/valid/tutorial/spatconv.html` (visited on 10/27/2022).

[109] L. Richardson, "The approximate arithmetical solution by finite differences of physical problems involving differential equations, with an application to the stresses in a masonry dam", Philosophical Transactions of the Royal Society of London. Series A, Containing Papers of a Mathematical or Physical Character **210**, 307–357 (1911).

[110] L. Richardson and J. Gaunt, "The deferred approach to the limit", Philosophical Transactions of the Royal Society of London. Series A, Containing Papers of a Mathematical or Physical Character **226**, 299–361 (1927).

[111] J. D. Craggs, "The collected works of irving langmuir", Physics Bulletin **13**, 86–87 (1962).

[112] W. Johnson and C. Silva, "Observations from exploration of VTOL urban air mobility designs", in , NTRS Author Affiliations: NASA Ames Research Center NTRS Report/Patent Number: ARC-E-DAA-TN60637 NTRS Document ID: 20180007847 NTRS Research Center: Ames Research Center (ARC) (Oct. 30, 2018).

[113] A. R. Kadhiresan and M. J. Duffy, "Conceptual design and mission analysis for eVTOL urban air mobility flight vehicle configurations", in *AIAA aviation 2019 forum*, _eprint: https://arc.aiaa.org/doi/pdf/10.2514/6.2019-2873 (American Institute of Aeronautics and Astronautics, 2019).

[114] D. F. Young, B. Munson, and T. Okiishi, eds., *A brief introduction to fluid mechanics*, 5th ed, OCLC: ocn667210577 (Wiley, Hoboken, NJ, 2011), 474 pp.

[115] World Meteorological Organization. Commission for Maritime Meteorology, *The beaufort scale of wind force : (technical and operational aspects)* (Geneva : WMO, 1970., 1970).

[116] *Helicopter flying handbook*, FAA-H-8083-21B (United States Department of Transportation, Federal Aviation Administration, 2019).

[117] E. Houghton, P. Carpenter, S. H. Collicott, and D. T. Valentine, "Propulsion devices", in *Aerodynamics for engineering students* (Elsevier, 2013), pp. 645–687.

[118] W. Z. Shen, M. O. L. Hansen, and J. N. Sørensen, "Determination of the angle of attack on rotor blades", Wind Energy **12**, _eprint: https://onlinelibrary.wiley.com/doi/pdf/10.1002/we.277, 91–98 (2009).

[119] S. K. Thomas, R. P. Cassoni, and C. D. MacArthur, "Aircraft anti-icing and de-icing techniques and modeling", Journal of Aircraft **33**, 841–854 (1996).

[120] R. Hann, "UAV icing: comparison of LEWICE and FENSAP-ICE for anti-icing loads", in AIAA scitech 2019 forum (Jan. 7, 2019).

[121] A. E. Albright, D. L. Kohlman, W. G. Schweikhard, and P. Evanich, *Evaluation of a pneumatic boot deicing system on a general aviation wing model*, KU-FRL-464-2, NTRS Author Affiliations: Kansas Univ., NASA Lewis Research Center NTRS Document ID: 19810016530 NTRS Research Center: Legacy CDMS (CDMS) (June 1, 1981).

[122] P. Pellicano and J. Riley, "Residual and inter-cycle ice for lower-speed aircraft with pneumatic boots", in 45th AIAA aerospace sciences meeting and exhibit (Jan. 8, 2007).

[123] R. Hann and N. Müller, *Icing validation database*, in collab. with R. Hann and N. U. O. S. bibinitperiod Technology, Type: dataset, 2020.

[124] Y. Liu and H. Hu, "An experimental investigation on the convective heat transfer process over an ice roughened airfoil", in 54th AIAA aerospace sciences meeting (Jan. 4, 2016).

[125] K. Ignatowicz, F. Morency, and H. Beaugendre, "Sensitivity study of ice accretion simulation to roughness thermal correction model", Aerospace **8**, 84 (2021).